
1

GROWTH OF BULK, THIN FILMS, AND NANOMATERIALS

1.1 INTRODUCTION

The evolution of the growth of the high quality semiconductor materials from bulk to nanomaterials enables researchers to fabricate devices with a continued enhancement of the properties and performance. In this chapter, the discussion is directed toward the growth of semiconductor single crystals by using various techniques ranging from bulk crystal growth to the epitaxial growth of quantum dots and core/shell nanocrystals. Bulk crystal growth techniques include liquid-encapsulated Czochralski (LEC), horizontal Bridgman (HB), liquid-encapsulated Kyropoulos (LEK), and vertical gradient freezing (VGF) methods. There are many improved methods available for the growth of bulk semiconductor crystals. For example, magnetic LEC, direct synthesis-LEC, pressure-controlled LEC, and thermal baffle LEC methods are all variations of the original LEC technique, but with improved growth conditions. Other bulk growth techniques include dynamic gradient freezing, horizontal gradient freezing, magnetic LEK, and vertical Bridgman methods. The widely used epitaxial growth techniques are the molecular beam epitaxy (MBE), metal–organic chemical vapor deposition (MOCVD) techniques, and liquid-phase epitaxy (LPE). The word *epitaxy* is a Greek origin composed of two parts, *epi* (placed or resting on) and *taxis* (arrangement). Thus, *epitaxy* refers to the formation of single-crystal nanomaterials on top of a substrate. The techniques used to grow bulk materials are usually equilibrium growth techniques, while the epitaxial growth techniques, used for the production of nanomaterials, are considered nonequilibrium techniques.

The growth techniques of bulk semiconductor crystals are designed to produce large-volume crystals under equilibrium conditions with almost no flexibility in the production of alloy composition. These techniques, however, lack the ability to produce heterojunctions, ternary or quaternary semiconductor compounds needed for advanced semiconductor devices. Silicon single-crystal boules as large as 12 in. (~ 300 mm) in diameters and over a meter in length are currently produced by LEC technique. GaAs single-crystal boule diameter is usually smaller than that of Si boules. Epitaxial growth is performed on submillimeter thick substrates cut from these bulk boules.

The process of preparing the boules into wafers that are used as substrates for epitaxial growth is called the *wafering process*. This process includes slicing, lapping, polishing, and cleaning. Since most wafers are used as substrates for epitaxial growth, the wafering process technology and the bulk crystal growth are very important for successful epitaxial growth. For example, the surface orientation accuracy, which is determined during the slicing process, affects the morphology of the epitaxial layer surface. Wafer flatness is another important parameter for high quality epitaxial growth. Single- or double-sided polished wafer flatness is defined by specific parameters, such as total thickness variation, total indicator reading, or focal plane deviation. These parameters are needed for precise photolithography. The surface roughness is also important aspect of the wafering process, since surface roughness in a subnanometer scale is required for many epitaxially grown nanomaterials.

Epitaxial growth, such as MBE and MOCVD growth, requires ready-to-use wafers. For example, thermal oxidation and/or ultraviolet/ozone oxidation processes have been effective in producing thin oxide layers, which protect the wafer surface. These oxide layers can be removed by heating prior to epitaxial growth. Packaging the wafers in nitrogen gas is an effective method against residual oxidation of polished surfaces during storage.

Crystallographic orientation of the wafers is very important for the MBE and MOCVD growth methods. The orientation is determined by Miller indices. These indices are defined as the smallest possible integers with the same ratios as the inverse of the intersection of a plane with a set of axes defined by the unit vectors of the crystal. An illustration of this concept is shown in Fig. 1.1 for a cubic crystal where a plane is intersecting x -, y -, and z -axes at a distance $2a$, $3a$, and $4a$, respectively, where a is the interatomic distance. To obtain the miller indices, one may follow the following steps: identify the intersections of the plane with the axes (in the case of Fig. 1.1, these intersections are 2, 3, and 4); take the inverse of these intercepts, which results in $1/2$, $1/3$, and $1/4$; find the smallest multiplier factor of the denominators, which 12; and multiply the factor the inverse of the intercepts to give 6, 4, and 3. These last numbers are called *miller indices*, and they are usually written in the following format (643) to indicate the crystallographic orientation of the wafers. If the intercept is negative, then the negative sign “-” is usually place on the top of the index. A group of Miller indices, such as (100), (010), (001), ($\bar{1}00$), (0 $\bar{1}0$), and (00 $\bar{1}$),

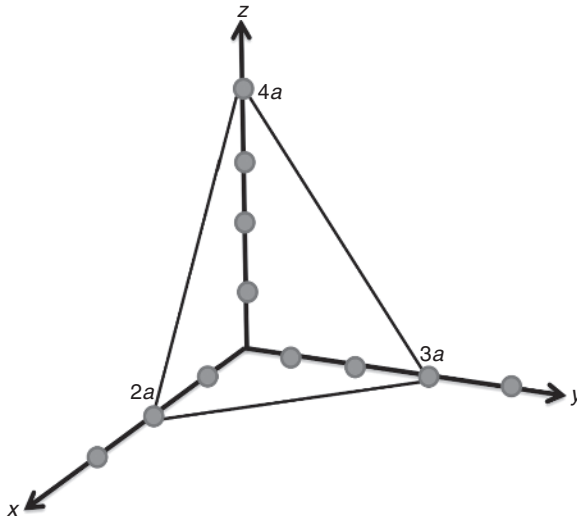


FIGURE 1.1 A plane intersecting the x -, y -, and z -axes at $2a$, $3a$, and $4a$, respectively, to determine the Miller indices. The interatomic distance is designated as “ a .”

is given the following notation $\{100\}$. For hexagonal crystal structure, the Miller indices are $(a_1a_2a_3c)$.

Most of the semiconductor materials are produced by artificial methods. Semiconductor binary, ternary, quaternary alloys (Fig. 1.2), heterojunctions, and other quantum structures such as superlattices and quantum dots are currently grown by two main epitaxial growth techniques, namely MBE and MOCVD. These growth techniques enable the synthesis of high quality single-crystal nanomaterials deposited layer by layer on suitable substrates.

Both equilibrium and nonequilibrium growth of semiconductors are based on chemical reactions. Furthermore, the thermodynamic analysis provides information about the feasibility of chemical reactions that can lead to the production of compound semiconductors. For example, the free energy function, G , can be written as

$$G = H - TS, \quad (1.1)$$

where H is the enthalpy, S is the entropy, and T is the temperature. For a system that is undergoing a chemical reaction, the change in the free energy can be written as

$$\Delta G = G_f - G_i = \Delta H - T\Delta S, \quad (1.2)$$

where G_i and G_f are the free energy of the initial and final states of the reaction, respectively. According to the second law of thermodynamics, “*in all energy exchanges, if no energy enters or leaves the system, the potential energy of the final state will always be less than that of the initial state,*” or $G_f < G_i$. Thus, the

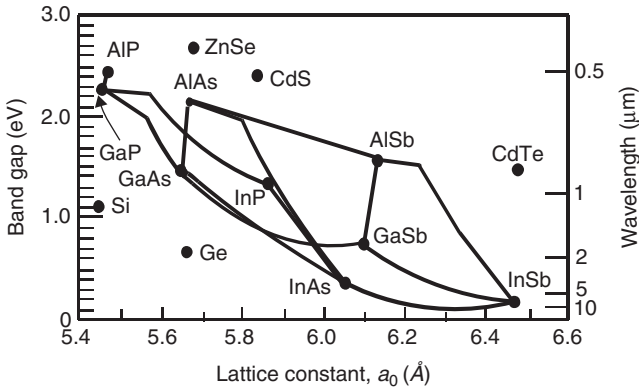


FIGURE 1.2 The band gap as a function of the lattice constant plotted for several binary semiconductors. Silicon and Germanium are also shown. The solid lines represent the ternary compounds.

system tends to minimize its free energy to a lower value than the initial state. For a forbidden process, we have $\Delta G > 0$, and for a system at equilibrium, the change in the free energy is zero ($\Delta G = 0$).

Let us consider the following chemical reaction between materials X and Y, which yields material Z,



where x , y , and z are called the *stoichiometric coefficients*. If one assumes that the materials X, Y, and Z are at equilibrium, then the change in the free energy is given by

$$\Delta G = zG_z - xG_x - yG_y. \quad (1.4)$$

The free energy of individual reactants is usually given as

$$G_j = G_j^0 + RT \ln a_j, \quad (1.5)$$

where j is the reactant (X, Y, or Z), a_j is called the *activity*, which reflects the change in the free energy when the material is not in its standard state, G_j^0 is the free energy of the j^{th} reactant in its standard state, and R is the gas constant [8.3143 J/(K/mol), 1.9872 cal mol⁻¹.K⁻¹, or 62.363 L mol⁻¹K⁻¹]. The standard state is defined as one atmospheric pressure for a gas at a temperature of 25°C. Substituting Equations (1.5) into (1.4) and solve for $\Delta G = 0$ to obtain

$$-\Delta G^0 = RT \ln k, \quad \text{where} \quad k = \frac{(a_Z)^z}{(a_X)^x (a_Y)^y}. \quad (1.6)$$

The values of a_j ($j = X, Y, Z$) are usually taken while the system is at the equilibrium.

In addition to the above simple thermodynamic description, the inspection of changes of composition of a material from one phase to another is usually accomplished by visualizing the phase diagram. The phase diagram helps understanding the chemical and physical properties of the material and how one can produce nanomaterials. For example, when a material fails to perform, one can refer to the phase diagram and deduce what might have happened to cause the failure. Then, one can revisit the thermodynamic laws that govern the phase diagram and extrapolate information.

1.2 GROWTH OF BULK SEMICONDUCTORS

Single-crystal growth of various bulk semiconductor materials has been performed by several methods, such as the LEC method, modified LEC methods, VGF methods, and HB methods. In this section, the most commonly used methods are discussed.

1.2.1 Liquid-Encapsulated Czochralski (LEC) Method

This growth method of bulk semiconductors was first developed by Czochralski in 1916. It uses what is called a *crystal puller* as illustrated in Fig. 1.3. The crystal puller consists of a high purity quartz crucible filled with polycrystalline materials, which are heated above their melting point by induction using radio frequency (RF) energy. The crucible holder is usually made of graphite. What is called a *seed*, or a small single crystal with a specific orientation is lowered into the molten material and then drawn upward using a pulling–rotation mechanism. The material in the melt makes a transition into a solid-phase crystal at the solid–liquid interface. The new solid-phase crystallographic structure is a replica of that of the seed crystal. During the growth process, the crucible rotates in one direction (12–14 rotations/min) while the seed holder rotates in the opposite direction (6–8 rotation per minute). At the same time, the boule is slowly pulled upward. The crystal diameter is usually monitored by an optical pyrometer, which is focused at the interface between the crystal (boule) and the melt. An automatic diameter control system maintains the desired crystal diameter through a feedback loop control. An inert gas such as argon is usually used as the ambient gas during the crystal-pulling process.

In the LEC crystal growth, boric oxide (B_2O_3) is used as an encapsulant to prevent the decomposition of the melt. Boric oxide is extracted as $Na_2B_4O_7$ solution from minerals including boron and then precipitated as boric acid (H_3BO_3). Boric acid is refined by repeated recrystallization and dehydrated by heating. The purity of boric oxide is very important since the impurities in boric oxide could contaminate the melt.

The molten semiconductor and solid are usually kept at the same pressure and have approximately the same composition. The crystallization resulted from a

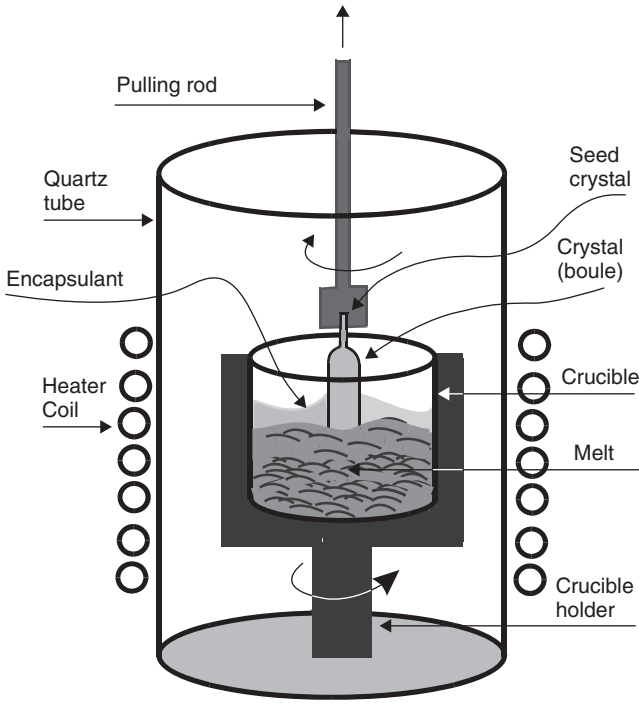


FIGURE 1.3 A illustration of a furnace (crystal puller) typically used in LEC single-crystal growth.

reduction in temperature; as the melt is pulled up, it loses heat by radiation and convection to the inert gas (for example, argon). The heat loss to the inert gas causes a substantial thermal gradient across the liquid–solid interface. Additional energy loss is due to solidification (latent heat of fusion). For a fixed volume, a one dimensional energy balance for the interface can be expressed as

$$\left[-k_l A \frac{dT}{dx} \Big|_l \right] - \left[-k_s A \frac{dT}{dx} \Big|_s \right] = L \frac{dm}{dt}, \quad (1.7)$$

where k_l and k_s are the thermal conductivities at the melting point of the liquid and solid, respectively, A is the boule's cross-sectional area, T is the temperature, L is the latent heat of fusion, m is the mass of the growing solid, and t is the time. Generally speaking, the heat diffusion from the liquid is small as compared to that from the solid. Thus, Equation (1.7) can be approximated by neglecting the first term on the left-hand side. With this approximation, one can express the maximum velocity, v_{\max} , at which the solid can be pulled as

$$v_{\max} \approx \frac{k_s A}{L} \frac{dT}{dm} = \frac{k_s}{M_v L} \frac{dT}{dx} \Big|_s, \quad (1.8)$$

where M_v is the solid density of the crystal being grown. If the crystal is pulled with a velocity larger than this maximum velocity, it will not conduct heat fast enough and the formation of a single crystal becomes difficult to achieve. In general, the pull rate of the *seed* crystal varies during the growth cycle. It is faster when growing the narrow neck so that the generation of dislocations is minimized and slower during the growth of the boule. Figure 1.4 shows a picture of 75-mm diameter and 240-mm long InP single-crystal grown by pressure-controlled LEC method (Oda *et al.*). The seed, neck, and shoulder of the crystal are indicated.

Crystals grown by LEC technique are susceptible to the incorporation of unwanted impurities. For example, quartz is used as a crucible when growing silicon crystals and the growth temperature is on the order of 1500°C. Thus, a small amount of oxygen will be incorporated into the boule. For extremely low concentration of oxygen impurities in silicon, the boule can be grown under the influence of a magnetic field. The magnetic field is usually directed perpendicular to the pull direction, where Lorentz force will change the motion of the ionized impurities in the melt in such a way as to keep them away from the liquid–solid interface. This configuration leads to a substantial decrease in the impurity incorporation in the crystal.

The LEC growth of compound semiconductors, such as GaAs and InP, is more difficult when compared to that of silicon crystals. For example, pyrolytic boron nitride (PBN) crucibles are used for compound semiconductors instead of quartz crucibles and B_2O_3 is used as encapsulant. The thermal conductivity of GaAs ($\sim 0.5 \text{ W}\cdot\text{cm}^{-1}\cdot\text{K}^{-1}$) is about one-third that of silicon ($\sim 1.4 \text{ W}/\text{cm}\cdot\text{K}$). Thus, GaAs cannot dissipate the latent heat of fusion as fast as silicon. Additionally, the shear stress required to generate a dislocation in GaAs at the melting point is about one-fourth that in silicon. These thermal and mechanical properties only permit the growth of 125-mm diameter GaAs boules as compared to that of silicon of 300 mm diameter. Furthermore, the GaAs boules contain defect densities a few orders of magnitude higher than those defect densities found in silicon boules.

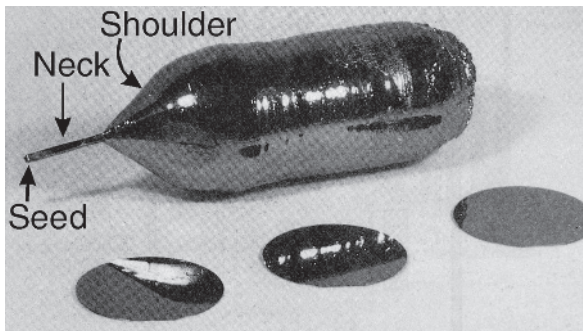


FIGURE 1.4 A 75-mm diameter and 240-mm long InP single-crystal grown by pressure-controlled LEC method (after Oda *et al.*).

In addition to the above difficulties of LEC semiconductor growth, there are other issues worth mentioning. One of them is called *stacking fault energy*. Small stacking fault energy promotes the formation of twins. This is the main reason why many of the compound crystals are difficult to grow as single crystals. An example is InP where twinning, which is more common in InP as compared to GaAs, is the main growth obstacle. The stacking fault energy in InP is smaller than those of GaAs or GaP. Another issue worth mentioning here is the sheer stress, which is a major factor in predicting the generation of dislocations. Most compound semiconductors have lower sheer stress as compared to that of silicon. Thus, the reduction of dislocation densities becomes a key issue for realizing high quality materials.

Doping single crystals during LEC growth is very important since it is desired to produce *n*-type, *p*-type, or semi-insulating substrates. For example, introducing boron or phosphorus into silicon melt produces *p*-type or *n*-type silicon, respectively. In the case of GaAs, the undoped or Cr-doped material is usually semi-insulating. Adding silicon as a dopant to GaAs produces *n*-type materials, while the addition of carbon or beryllium produces *p*-type GaAs. During LEC growth, the dopant concentration in the boule is usually different from the dopant concentration in the melt. The ratio between the two concentrations is known as the *equilibrium segregation coefficient*, k_0 , which expressed as

$$k_0 \equiv \frac{C_s}{C_l}, \quad (1.9)$$

where C_s and C_l are the equilibrium dopant concentrations in the solid and liquid in the vicinity of the interface. Usually k_0 is less than unity. For example, k_0 values for B and P dopants in silicon are 0.80 and 0.35, respectively, while the values of k_0 for Si and C dopants in GaAs are 0.185 and 0.8, respectively.

It is desired to obtain an expression for the dopant concentration in the solid crystal as it is pulled out of the melt during the LEC growth. Assume that the initial crystal weight and dopant concentration in the crystal are m_0 , C_s , respectively. Also, assume that the amount of dopants by weight remaining in the melt is σ when the crystal weight increases to m during growth. When the crystal weight increases by the amount dm , the corresponding reduction of the dopant weight from the melt is

$$-d\sigma = C_s dm. \quad (1.10)$$

On the other hand, the remaining weight of the melt is $(m_0 - m)$. Hence, the doping concentration in the liquid, C_l , is given by

$$C_l = \frac{\sigma}{m_0 - m}. \quad (1.11)$$

By combining Equations 1.9–1.11, the reduction of the dopant (by weight) in the melt can be written as

$$\frac{d\sigma}{\sigma} = -k_0 \frac{dm}{m_0 - m}. \quad (1.12)$$

Integrate Equation (1.12) using $C_0 m_0$ and σ for the initial and final weights of the dopant in the melt, respectively, and the initial and final weights of the crystal are 0 and m , respectively. The final result is given as

$$C_s = k_0 C_0 \left[1 - \frac{m}{m_0} \right]^{k_0 - 1}. \quad (1.13)$$

A plot of C_s versus m for different values of k_0 is left as an exercise. Notice that C_0 is the initial dopant concentration in the melt. For $k_0 = 1$, we have a constant concentration profile. On the other hand, C_s increases as m is increased for $k_0 < 1$, while C_s decreases as a function of m for $k_0 > 1$. Equation (1.13) tells us that there is a concentration gradient along the length of the crystal. In other words, the dopant concentration near the seed is different than that near the tail of the crystal. There is also a radial gradient dopant concentration. In other words, the dopant concentration near the center of the boule is different than that near the rim. Usually, the mapping of dopant concentration across the wafer using techniques, such as photoluminescence or absorption at a fixed wavelength, is very helpful in determining the carrier concentration in wafers.

The segregation coefficient may not be constant for dopants in LEC-grown semiconductor materials. The segregation coefficient discussed above is derived for the system near the liquid–solid interface. Away from this interface, the segregation coefficient can be different. To derive an expression for the effective segregation coefficient, let us assume that the dopant distributions in the solid and liquid phases are given by the profiles shown in Fig. 1.5 (see Ohring). As mentioned earlier, the segregation coefficient at equilibrium is defined near $x = 0$ as $k_0 = C_s/C_l(0)$. However, one can define the effective segregation coefficient, k_e , as the ratio between C_s and C_l , where C_l is the dopant concentration away from the solid–liquid interface. Now, let us consider small layer of the melt with width ϵ , in which the only flow is that required to replace the crystal being withdrawn from the melt, as shown in Fig. 1.5. Outside this layer, the dopant concentration is almost constant with a value of C_1 , while inside the layer, the dopant concentration, $C(x)$, can be described by the steady-state continuity equation as

$$v \frac{dC(x)}{dx} + D_d \frac{d^2 C(x)}{dx^2} = 0, \quad (1.14)$$

where v is the velocity at which the crystal is being pulled out the melt (Eq. (1.8)), and D_d is the dopant diffusion coefficient. A possible solution of this equation is

$$C(x) = A e^{-vx/D_d} + B, \quad (1.15)$$

where A and B are constants that need to be determined from the boundary conditions. The first boundary condition is $C(x) = C_1(0)$ at $x = 0$, which gives

$$C_1(0) = A + B. \quad (1.16)$$

The second boundary condition is that the sum of the dopant fluxes at the interfaces must be zero, which yields

$$D_d \frac{dC(x)}{dx} \Big|_{x=0} + (C_1(0) - C_s)v = 0. \quad (1.17)$$

Substituting Equations (1.15) into (1.17) gives

$$A = (C_1(0) - C_s). \quad (1.18)$$

Combining Equations (1.15), (1.16), and (1.18) yields

$$C(x) = (C_1(0) - C_s)(e^{-vx/D_d} - 1) + C_1(0). \quad (1.19)$$

From Fig. 1.5, one can see that $C(x) \approx C_1$ at $x = \epsilon$. Thus, Equation (1.19) becomes

$$e^{-v\epsilon/D_d} = \frac{(C_1 - C_s)}{(C_1(0) - C_s)}, \quad (1.20)$$

which yields

$$k_e \equiv \frac{C_s}{C_l} = \frac{k_0}{k_0 + (1 - k_0)e^{-v\epsilon/D_d}}. \quad (1.21)$$

A plot of Equation (1.21) is shown in Fig. 1.6 for different values of the growth parameters ($v\epsilon/D_d$) ranging from 0 to 10. For low values of $v\epsilon/D_d$ and $k_0 < 1$,

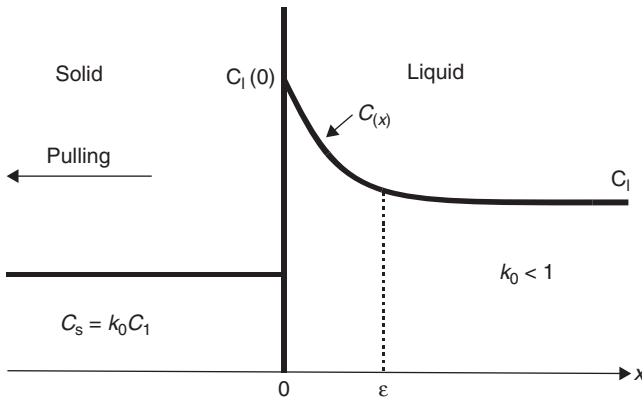


FIGURE 1.5 The distribution of a dopant near the solid–liquid interface in LEC crystal.

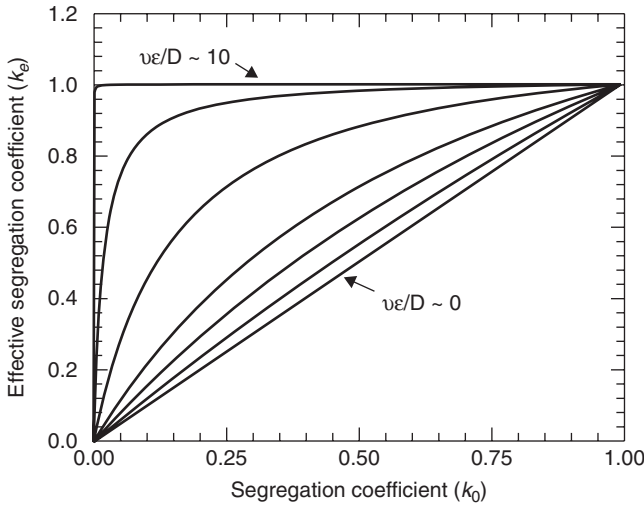


FIGURE 1.6 The effective segregation coefficient, k_e , is plotted as a function of k_0 for different values of $\nu\epsilon/D_d$.

the effective segregation coefficient is approximately the same as k_0 , but it is always larger than k_0 and approaches unity for large values of $\nu\epsilon/D_d$. Thus, a uniform doping distribution, where k_e approaches unity, in the crystalline solid can be achieved by increasing the pull maximum velocity and a low rotation speed. Owing to the centripetal force, the rotation speed is inversely proportional to ϵ .

1.2.2 Horizontal Bridgman Method

As the case of LEC growth method, the HB growth method needs a crystal seed. This growth technique consists of melt, crystal, and seed, which all kept inside a crucible during the entire heating and cooling processes. This technique is illustrated in Fig. 1.7, where two variations of the same method are presented. In the case of silicon growth using Bridgman method, a quartz crucible filled with polycrystalline material is placed inside a furnace tube and the heater is pulled. As the heater is drawn slowly away from the seed (Fig. 1.7a), the polycrystalline material is melted near the seed. The heater continues to move away from the seed's region, the molten material solidifies into a single crystal with a crystallographic structure similar to that of the seed. The shape of the resulting crystal is determined by the shape of the crucible. Another variation of this growth technique is shown in Fig. 1.7b, where the crucible is pulled slowly from the heater region into a colder region. The seed crystal induces single-crystal growth.

The drawback of Bridgman growth method is that the material is constantly in contact with the crucible, which produces two effects. First, the silicon crystals tend to adhere to the crucible, and second, the crucible wall introduces stress in

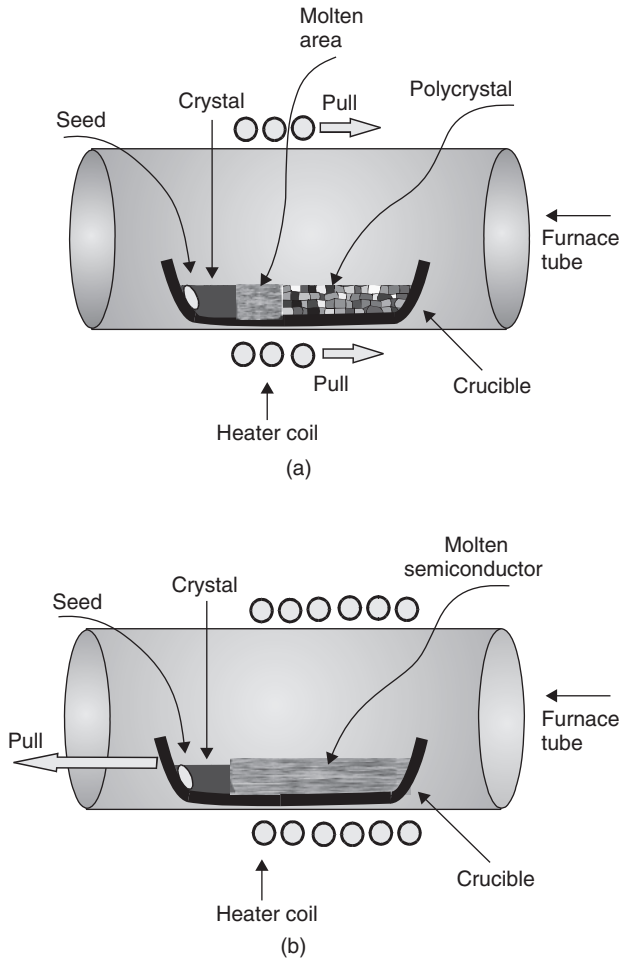


FIGURE 1.7 Schematic diagrams of the horizontal Bridgman growth method. (a) The heater is pulled over the polycrystalline material causing it to melt. As the heater moved away from the seed's region, the molten material solidifies into a single crystal. (b) A variation of Bridgman method, where the crucible is pulled away from the heater region.

the solidifying crystal. The presence of stress causes deviations from the ideal crystal structure.

The growth of compound semiconductors using Bridgman method is somewhat different than the growth of silicon crystals. For example, the growth of GaAs crystals is illustrated in Fig. 1.8a. In this growth method, both gallium and arsenic are loaded onto a fused silica ampoule, which is then sealed. The addition of the solid arsenic in the chamber provides the overpressure necessary to maintain stoichiometry. The furnace tube is slowly pulled past the charge (the charge is a term used to describe the semiconductor components that are placed in the

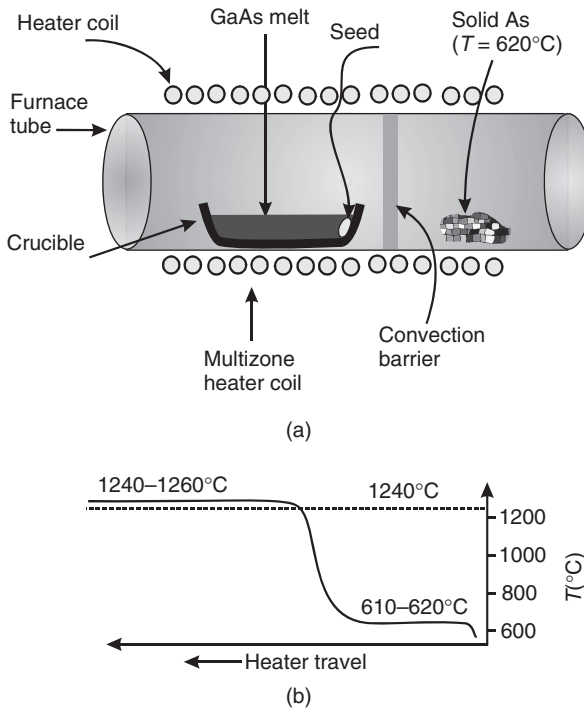


FIGURE 1.8 (a) A schematic diagram of the horizontal Bridgman growth method for GaAs and other compound semiconductors. (b) A sketch of the temperature for two-stage furnace.

crucible). The temperature of the furnace is set to melt the charge when it is completely inside the furnace. As the furnace is pulled past the ampoule, the molten GaAs charge recrystallizes with a structure similar to that of the seed crystal.

The heater coil in the Bridgman growth method is actually a multizone furnace. Figure 1.8b shows the temperature as a function of the direction of the heater travel for a two-stage heater. The first stage (on the right) is kept at about $610\text{--}620^\circ\text{C}$ to maintain the required overpressure of arsenic. The second stage (on the left) is held at about $1240\text{--}1260^\circ\text{C}$, which is just above the melting point of GaAs ($\sim 1240^\circ\text{C}$). It is possible to grow GaAs with this method using GaAs polycrystalline as the charge (the starting material) instead of gallium and arsenic components.

Compound semiconductor boules grown by HB method are usually ~ 50 mm in diameter, which is small as compared to those boules grown by LEC method. However, with precise control of the stoichiometry and the radial and axial temperature gradients, a large boule size can be grown. The advantage of the HB method is that the dislocation densities in materials, such as GaAs, is of the order

of 10^3 cm^{-2} , which is about an order of magnitude smaller than the dislocation densities found in LEC-grown material.

1.2.3 Float-Zone Growth Method

The float-zone growth method is mostly used to grow high purity silicon boules directly from a high purity rod of polycrystalline material obtained from other methods such as purification processes. With this growth method, a background carrier concentration lower than 10^{11} cm^{-3} can be easily achieved. Compound semiconductor materials are not generally grown by this technique. A schematic of the float-zone growth apparatus is shown in Fig. 1.9. A seed crystal is attached at the bottom of the polycrystalline rod in a vertical position. The rotating polycrystalline rod is enclosed in a quartz tube. An inert gas (argon) flows in the tube such that a one atmospheric pressure is maintained during growth. A small

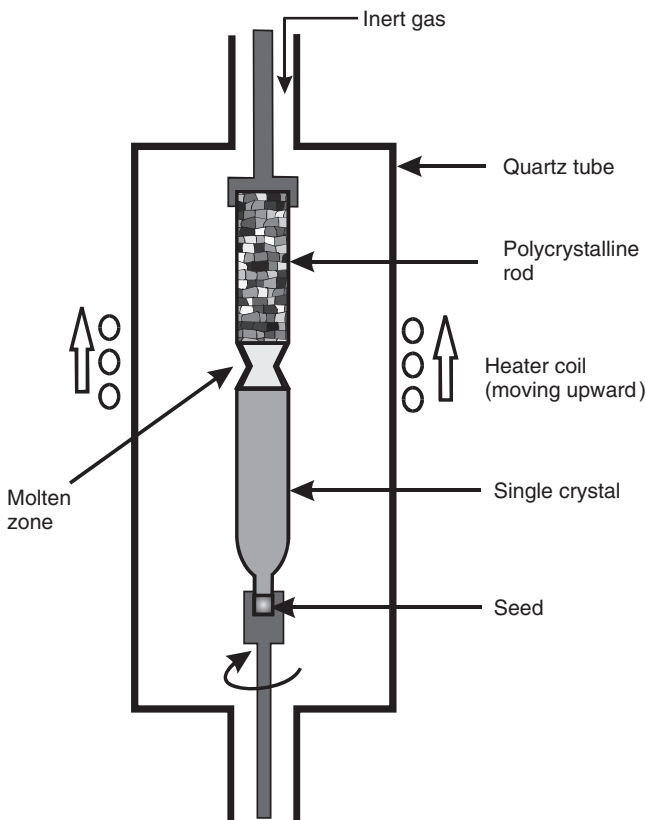
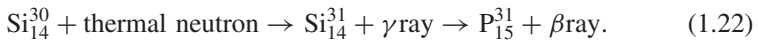


FIGURE 1.9 A cross-section of the float-zone apparatus used to grow silicon single crystals.

region of the polycrystalline rod is melted by passing an RF heater, which is moved upward from the seed. A float zone (a few centimeters in length) of melt is formed between the seed crystal and the polysilicon rod and retained by the surface tension between the melting and the growing solid phases. The molten zone that solidifies first remains in contact with the seed crystal retaining the same crystallographic structure of the seed. As the molten region is moved along the length of the polycrystalline rod, the rod melts and then solidifies throughout its entire length, it becomes a single crystal. The motion of the heater controls the diameter of the crystal.

Difficulties in preventing the molten zone from collapse have limited the float-zone method to growing small diameter crystals. The maximum crystal diameter is on the order of 70 mm. However, one of the advantages of this technique is that there is no crucible involved, so oxygen contamination is eliminated. Another advantage of this growth method is that the background impurities can be substantially reduced by passing the heater coil over the crystal several times. The background impurities can be reduced by a few orders of magnitude when the heater coil is passed over the crystal seven or eight times (see Pfann).

The introduction of doping in the growth method is more difficult when compared to the LEC and Bridgman growth methods. There are four techniques used to introduce dopants in float-zone growth method. First, core doping is based on the introduction of doped polysilicon as the starting material. Second, gas doping is based on the injection of gases, such as AsCl_3 , BCl_3 , or PH_3 , into the polysilicon rod as it is being deposited or into the molten zone region during refining. Third, pill doping is based on the insertion of a small pill of dopant, such as gallium or indium, into a hole from at the top of the polysilicon rod. Dopants with small segregation coefficients will diffuse into the rod as the melt passes over the polysilicon rod. Fourth, neutron transmutation doping is based on irradiating the silicon single crystal by thermal neutrons. This process produces a fractional transmutation of silicon into phosphorus, which leads to n -type silicon. The neutron transmutation equation is given by



The life time of the intermediate Si_{14}^{31} is 2.62 h. Neutron transmutation doping is very uniform since thermal neutrons penetration length in silicon is ~ 100 cm.

The doping distribution in the float-zone process can be understood by considering the model illustrated in Fig. 1.10. Assume that the initial uniform doping concentration in the rod is C_0 , L is the length of the molten zone at a distance x along the rod, A is the cross-sectional area of the rod, ρ is the specific density of silicon, and σ is the dopant concentration in the molten zone. When the molten zone is moved a distance dx , the amount of dopant added to it at its advancing end can be expressed as $C_0\rho A dx$, while the amount of dopant removed at the retreating end is $k_e\sigma dx/L$. The differential amount of dopant, $d\sigma$, remaining in

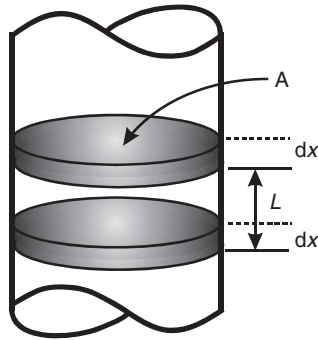


FIGURE 1.10 A sketch of a portion of a semiconductor boule used to illustrate the calculation of the doping profile.

the molten zone as it moves a distance dx can be expressed as

$$d\sigma = C_0\rho A dx - \frac{k_e\sigma}{L}dx, \quad (1.23)$$

which can be rewritten as

$$\int_0^x dx = \int_{\sigma_0}^{\sigma} \frac{d\sigma}{C_0\rho A - k_e\sigma/L}, \quad (1.24)$$

where σ_0 is the amount of dopant in the molten zone when it was first formed at the front end of the rod and is given by $C_0\rho AL$. An expression for the dopant concentration in the crystal at the retreating end is given by

$$C_s = \frac{k_e\sigma}{A\rho L}. \quad (1.25)$$

An expression can be obtained for σ by integrating Equation (1.24), which can be substituted into Equation (1.25) to yield the following relation

$$C_s = C_0\{1 - (1 - k_e)e^{-k_ex/L}\}. \quad (1.26)$$

A plot of this equation is left as an exercise. For small values of k_ex/L , C_s is nearly constant.

1.2.4 Lely Growth Method

The growth techniques discussed earlier could not be employed to grow wide band gap materials such as GaN and SiC. This is due to the fact that these materials do not have a liquid phase under reasonable thermodynamic conditions. The

growth conditions of the materials require high temperature and high pressure environment. For example, SiC melt exists only at pressures in the excess of 10^5 atmosphere and temperatures higher than 3200°C . Under these extreme conditions, the stoichiometry and stability of the melt are difficult to maintain. Silicon carbide material is grown by Lely method, which is schematically shown in Fig. 1.11a. The growth process is driven by a temperature gradient, which is maintained between the outer and inner areas of the crucible. The system is kept near equilibrium with lower partial pressures of the SiC precursor in the inner and colder zone. The two areas are separated by a porous graphite material, which provides nucleation centers. Since the inner region is colder, the chemical gradient causes a mass transport from the outer region to the inner region. Single crystals of SiC start to nucleate on the inner side of the porous graphite. As

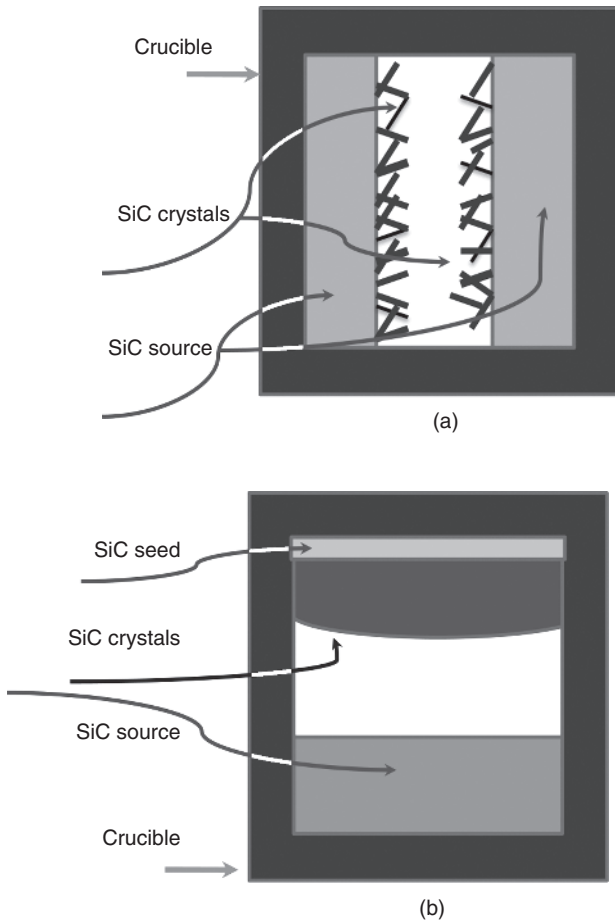


FIGURE 1.11 (a) A cross-sectional diagram of a cylindrical crucible for the Lely growth of SiC. (b) A cross-sectional diagram of the modified Lely growth technique.

illustrate in Fig. 1.11a, the crystals are limited in size with random dimensions, but nonetheless, they are of a high quality in terms of low defect densities. Atypical size of these crystals is ~ 1 cm, but they are used as seed crystals for other bulk SiC growth techniques including the modified Lely method described below.

The modified Lely method is based on a seeded sublimation growth or physical vapor transport technique. It is basically similar to the Lely method except that a SiC seed crystal is used as shown in Fig. 1.11b to achieve a controlled nucleation. According to Fig. 1.11, the cooler seed is placed at the top to minimize falling contaminations. Polycrystalline SiC source is heated to $\sim 2600^\circ\text{C}$ at the bottom of the crucible and sublimates at low pressure. Mass transport of SiC occurs and recrystallizes through supersaturation at the seed. The disadvantages of this technique include the poor control of the polytype and shape of the crystals, nonuniform doping, and high density of defects. Furthermore, the screw dislocations have been one of the long-standing problems of commercial bulk SiC wafers. This class of dislocations, which are also known as *nano- or micropipes*, can be closed or hollow. These micropipes have detrimental effects on SiC-based devices.

1.3 GROWTH OF SEMICONDUCTOR THIN FILMS

The growth of thin films requires finely polished substrates (wafers) cut from single-crystal boules grown by bulk crystal growth methods described in the previous sections. The growth of thin films, quantum wells, superlattices, quantum wires, and quantum dots requires a precise knowledge of the crystallographic structure of the substrates. Silicon substrates are used in the vast majority of silicon-based devices and technology. Silicon also has been used as a substrate for GaN-based devices because of its favorable physical properties, high quality, large sizes, and above all low cost. It has a diamond structure, which can be seen as two interpenetrating face-centered cubic sublattices with one sublattice displaced from the other by one-quarter of the distance along the diagonal of the cube. Each atom in the lattice is surrounded by four equivalent nearest neighbors that lie at the corners of a tetrahedron. The three commonly used structural orientations of Si are shown in Fig. 1.12.

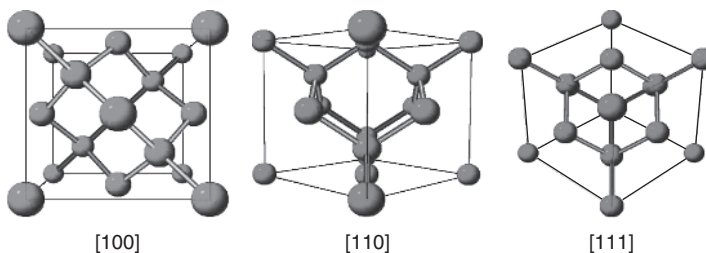


FIGURE 1.12 Views of the three commonly used crystallographic directions of Si wafers.

Gallium arsenide-based technology, which includes both electronic and optoelectronic devices, has been advancing rapidly since the epitaxial growth is mature for many III–V semiconductor nanomaterials. The reason for this advancement is the availability of GaAs substrates with many structural orientations. Gallium arsenide single crystal has a zincblende structure. A view of the main three structural orientations is shown in Fig. 1.13. Recently, GaAs substrates have been used for the growth of III-nitride materials. However, because the relatively low melting point of GaAs, it is less stable when compared to SiC and sapphire substrates.

1.3.1 Liquid-Phase Epitaxy Method

The LPE growth method is basically a precipitation of materials from supercooled solution onto a substrate. The LPE reactor is shown in Fig. 1.14, which consists of a horizontal furnace system and a sliding graphite boat. An enlarged illustration

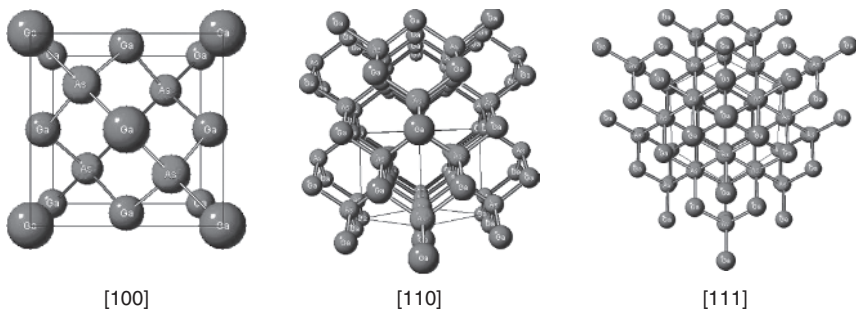


FIGURE 1.13 A view of three different structural directions of GaAs, which has a zincblende crystal structure.

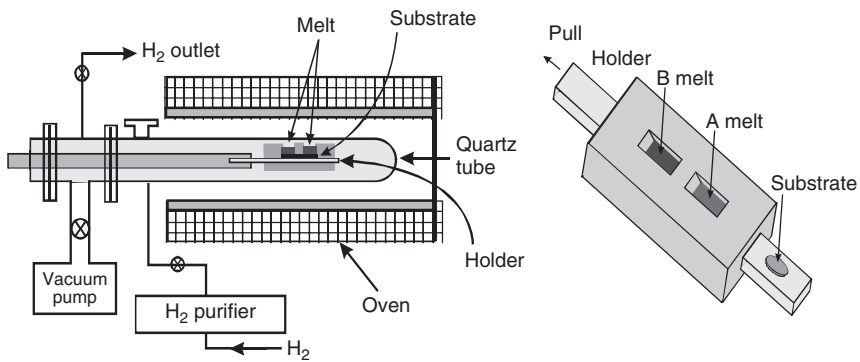


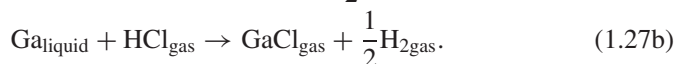
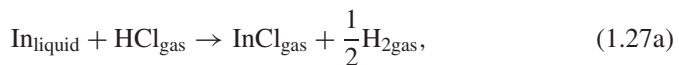
FIGURE 1.14 A cross-section of the liquid-phase epitaxy reactor. The illustration on the right is an enlarged crucible showing the melts and the substrate on the holder, which slides under the melt.

of the sliding graphite boat is shown on the right-hand side of Fig. 1.14, where two different melts A and B are used as an example of which a heterojunction can be made. If the melt A is GaAs, the melt B is AlGaAs, and the substrate is semi-insulating GaAs, then a GaAs/AlGaAs heterojunction can be grown with this technique. This simple reactor usually produces high purity thin films. The epitaxial growth processes in this technique are usually maintained at thermodynamic equilibrium. The composition of the thin films depends mainly on the equilibrium phase diagram of the material and to a lesser extent on the orientation of the substrate. The molten material is placed in a graphite boat and is slid inside the heated furnace of a suitable atmosphere. A subsequent cooling causes the solute to come out and deposit on the underlying substrate forming, an epitaxially grown layer. Growth using the LPE method is affected by the melt composition, growth temperature, and growth duration.

The advantages of the LPE method are the simplicity of the equipment used, higher deposition rates, low defect concentrations, excellent control of stoichiometry, and high purity materials. Background impurities are minimized by using high purity melt materials and by the inherent purification process that occurs during the liquid-to-solid-phase transition. Disadvantages, on the other hand, include poor thickness uniformity, high surface roughness, melt back effect, and high growth rates, which prevent the growth of multilayer structures, such as multiple quantum wells and superlattices, with abrupt interfaces. Additionally, only small size wafers can be used with the LPE method, which makes it a small-scale process. Contrary to the growth materials from the melt, LPE grown materials are temperature independent and thermal gradients are usually neglected.

1.3.2 Vapor-Phase Epitaxy Method

The name vapor-phase epitaxy (VPE) implies that the growth of thin films is based on reactive compounds in their gaseous form. The recent development of III-nitride materials renewed the interest in the VPE growth method. This growth technique is performed at thermodynamic equilibrium. A generic sketch of the VPE reactor is shown in Fig. 1.15 (see Razeghi). As shown in the figure, the reactor consists of a quartz tube (chamber), gas inlets, exhaust, and a furnace with different temperature zones. Three zones are shown in the temperature trace, which are called *synthesis*, *pyrolysis*, and *growth zones*. The growth of InP and GaAs samples is taken as an example. The gaseous species for the group III source materials are synthesized by reacting hydrogen chloride gas with a melted pure metal placed in crucibles. This process occurs in the first zone, the synthesis zone, which is maintained at temperature, T_s , of 750 and 850°C for GaAs and InP, respectively. The reaction between the metals and hydrogen chloride results in group III-chloride vapor compounds as follows



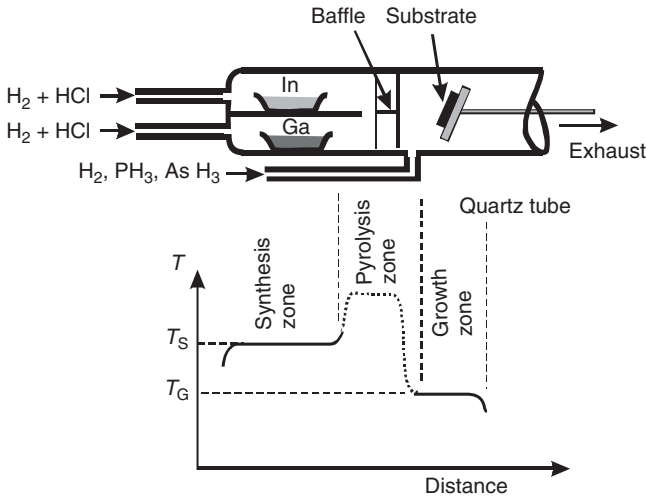
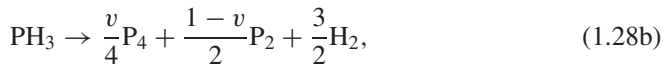
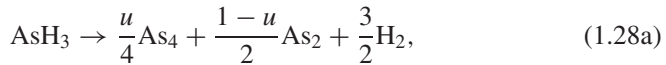


FIGURE 1.15 A cross-section of a vapor-phase epitaxy reactor with a multitemperature zones heater.

The group V source materials are provided in the form of hydride gases, such as arsine (AsH_3) and phosphine (PH_3). The hydride gas is pyrolyzed in the second zone, which is maintained at temperatures $T > T_s$. The decomposition of group V can be described as follows



where u and v are the mole fractions of AsH_3 and PH_3 that are decomposed into As_4 and P_4 , respectively.

The gas flow is cooled by a temperature gradient between the second and the third zones. The cooling of reactants results in the growth of semiconductor materials, such as GaAs and InP, on the substrate in the growth zone. The growth zone is maintained at temperatures, T_G , of 680 and 750°C for GaAs and InP, respectively. It is clear from the above equations that there are several chemical reactions taking place in the VPE reactor. These reactions can be classified as heterogeneous reactions, which occur between solids and liquids, solids and gases, and liquids and gases and homogeneous reactions that occur in the gas phase. During the steady-state film growth, the overall growth process is limited by the heterogeneous reactions, whereas the change in the composition of the grown semiconductor in the process (for example, switching the growth from InP to InGaAs) is limited by the mass transport in the gas phase.

The advantages of the VPE method include high deposition rate, multi-wafer growth, flexibility in introducing dopants into the materials, and good control of

the composition gradients by accurate control of the gas flows. The disadvantages include difficulties in growing multilayer quantum structures, potential formation of hillocks and haze, and interfacial decomposition during the preheat stage.

The renewed interest in the VPE method stems from its ability of high deposition rates under reasonable growth conditions. This advantage has been used for the growth of thick GaN films, on the order of 100 μm or thicker, where native bulk substrates are not available. The idea here is to replace the current substrates, which are mainly sapphire and SiC, by producing thick GaN films that can be used as compliant (quasi) substrates. The thick GaN films can be grown on other substrates, such as sapphire, then lifted and used as substrates in other growth techniques, such as the MBE and MOCVD techniques. The VPE growth of GaN utilizes hydrogen chloride gas that passes over a crucible containing metallic gallium at a temperature of $\sim 850^\circ\text{C}$ to form gaseous GaCl. Ammonia (NH_3) and HCl are then injected into the hydride pyrolysis zone using N_2 as a carrier gas. Gallium chloride is injected through a showerhead into the growth zone, which is kept at temperatures in the range of $950\text{--}1050^\circ\text{C}$. Gallium chloride then reacts with NH_3 on the substrate surface to produce GaN according to the following reaction



The $\text{NH}_3:\text{HCl}$ ratio is typically 30:1 with a growth rate of $\sim 0.3 \mu\text{m}/\text{min}$. There are, however, problems associated with the VPE growth of GaN. First, it is quite possible for NH_3 to dissociate and react with HCl to produce NCl_3 , which is highly explosive. Second, HCl can potentially causes leaks in the reactor. Third, undesired by-products such as NH_3Cl and GaCl_3 can clog the exhaust system unless heated to temperatures higher than 150°C . Fourth, because of the exchange reactions with the quartz chamber walls of the reactor, AlGaN growth and p-type-doped GaN are difficult to realize.

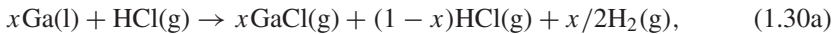
1.3.3 Hydride Vapor-Phase Epitaxial Growth of Thick GaN Layers

The hydride vapor-phase epitaxy (HVPE) is essentially a variation of the VPE method, but it has been developed to grow thick GaN films (for further details on the subject, see Paskova *et al.*). The increasing interest in III-nitride materials and devices has led to the long-standing demand for GaN substrates for homoepitaxy of GaN, which has yet to be satisfied. There are substantial difficulties in growing large-volume GaN single crystals at the high equilibrium vapor pressure of N_2 and the high growth temperature needed in bulk growth from Ga solution. Currently, there are three promising techniques that can be used to obtain GaN bulk crystals—high pressure crystal growth from Ga solution, the sublimation technique, and HVPE growth.

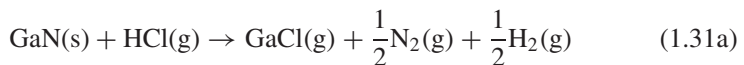
HVPE growth of thick GaN layers was developed by several research groups to provide quasi-bulk thick GaN layers. GaN layers with a thickness of several

hundred micrometers have been achieved in HVPE atmospheric pressure reactors at temperatures of about 1050°C and at a reasonable cost. The deposition process of GaN for substrate application requires a high growth rate and the ability to produce low defect material, since the threading defects are likely to extend into the subsequently grown epilayers. The growth rates in HVPE have been reported to be as high as 100 μm/h with a crystalline quality comparable to the best quality reported for MOCVD-grown GaN films. Several substrate pretreatments such as a GaCl sapphire pretreatment, a sapphire nitridation pretreatment, different buffer layers such as ZnO, reactive sputtered AlN, MOCVD-grown GaN, and epitaxial lateral overgrowth technique have greatly improved the quality of thick HVPE-GaN films. Despite rapid progress in the HVPE technique, a number of basic issues remain to be solved. One of them is the presence of a high density of extended defects such as dislocations, domain boundaries, and cracks. Efforts to further develop the HVPE-GaN thick layers for substrate use are concentrated on two main issues. The first is focused on the reduction of defect density and the control of the initial stage of the growth, which is the source for most defects. Secondly, an optimal procedure for subsequent removal of the foreign substrate from the GaN layer is far from complete, although very intense investigations of chemical, reactive ion etching, laser-induced liftoff, and polishing separation have been reported in the literature.

The basic HVPE reactions that describe the GaN deposition process can be written as follows:



where l is liquid, g is gas, s is solid, and x is the mole fraction of HCl reacting in the process. Notice that Equation (1.30bb) is the same as Equation (1.29). The GaN deposition is determined by the efficiency of both chemical reactions. Values of x in reaction (Eq. 1.30a) were found to be in the range from 0.70 to 0.86 depending on the temperature, the position of the HCl inlet, the carrier gas ambient, and the liquid Ga surface exposed to the HCl gas. The chemical reaction (Eq. 1.30b) depends on the fraction of ammonia not decomposed into nitrogen and hydrogen, since GaN cannot be formed by direct reaction between GaCl and N₂. It is known that ammonia is a thermodynamically unstable gas at the temperatures employed in the GaN growth. Fortunately, the thermal decomposition of NH₃ is a very slow reaction, and when no catalyst is present, no more than about 4% of the NH₃ is typically decomposed at temperatures higher than 950°C. Equation 1.30a, 1.30b is accompanied by GaN decomposition via the following two reactions:



These decomposition reactions are unlikely to occur in the growth temperature range of 950–1150°C.

The basic design of the HVPE reactor is similar to the VPE reactor with some modifications as shown in Fig. 1.16. These modifications can be summarized into two groups: horizontal and vertical reactor design. The horizontal reactor shown in Fig. 1.16a typically has five main temperature zones. In the first upstream zone, HCl reacts with metallic Ga forming GaCl and H₂. The area of the liquid Ga source is increased as much as allowed (typically 10–100 cm²) to achieve a large reactive Ga surface area for efficient GaCl production. The optimum temperature in the first zone is about 850°C. The second zone may be used for other metallic sources, such as In or Al when needed, or for dopants. The temperature of the third zone is kept in the range of about 1000–1060°C where GaCl and NH₃ are introduced and mixed. The substrate holder is placed in the fourth region of the reactor where the temperature is kept at ~1080°C. The most

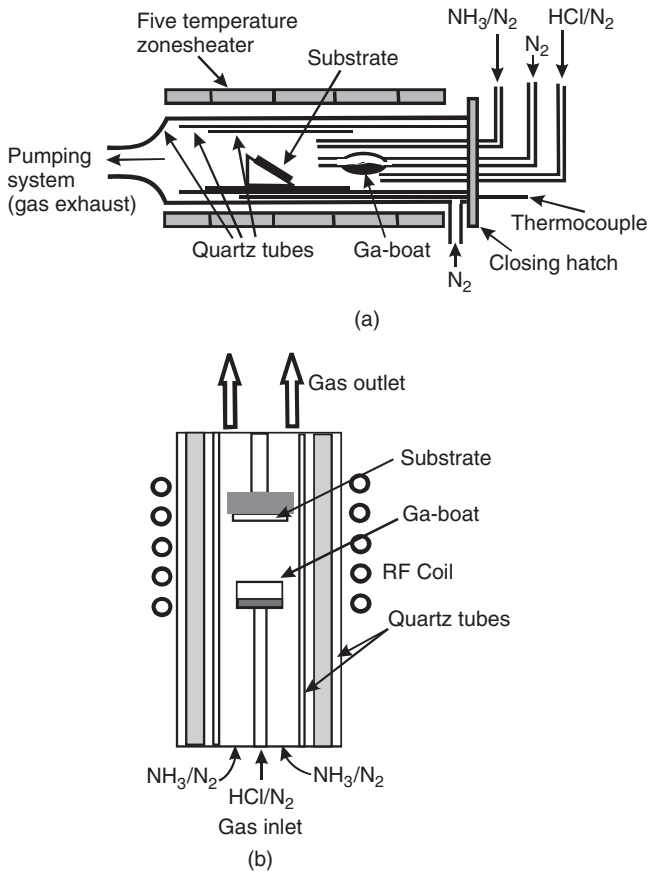


FIGURE 1.16 A schematic diagrams of (a) horizontal and (b) vertical HVPE reactors.

common method of heating in this design is resistive heating. The horizontal reactors utilize a susceptor that is situated approximately parallel to the gas flow direction. Uniform growth can be improved by tilting the substrate holder to eliminate reactant depletion along the flow direction. Another approach used in some horizontal reactors is the rotation of the substrate holder.

In the vertical design, the reactants are typically introduced through the top. The substrate is held flat on a susceptor that is perpendicular to the gas flow direction. The vertical reactor design facilitates substrate rotation during the growth to improve film uniformity. Heating is accomplished by resistance or RF induction, and temperature monitoring is accomplished by an infrared pyrometer or a thermocouple. An alternative modification is an inverted vertical reactor as shown in Fig. 1.16b, where the process gases are supplied through the bottom inlet flange, while the top flange can be lifted for loading and unloading. The substrates are placed in the upper part where the gases are mixed. The inverted reactor keeps all advantages of the vertical design and also provides the possibility for raising the substrate holder. An additional advantage of the inverted vertical reactor is the significant reduction of solid particle contamination.

1.3.4 Pulsed Laser Deposition Technique

The pulsed laser deposition (PLD) is a relatively new technique widely used for the growth of oxide thin films, such as ferroelectrics and superconductors (for detailed discussion, see Huang and Harris). There are, however, several advantages of the PLD for depositing high quality thin films and make it worthy of study as a method of growing III-nitride materials. One of these advantages is the simplicity of the technique. PLD is typically accomplished with a high power pulsed laser beam irradiating a bulk stoichiometric target. Through the interaction of the laser beam with the target, a forward-directed flux of material is ejected. A plasma is formed which is then transported toward a heated substrate placed directly in the line of the plume. This is illustrated in Fig. 1.17. The congruent ablation achieved with short laser pulses enables stoichiometric composition transfer between targets and films and allows deposition of multi-component materials by employing a single target. This feature makes the PLD the best initial investigation tool for complex materials because the stoichiometry control is vastly easier.

A useful feature of the PLD method is that multiple targets can be loaded inside the chamber on a rotating holder, which can then be used to sequentially expose different targets to the laser beam, thereby enabling *in situ* growth of heterostructures and superlattices with relatively clean interfaces. Virtually, any material can be laser evaporated, leading to the possibility of multilayers of a variety of materials. Therefore, PLD is suitable for rapid exploration of new materials-integration strategies for developing heterostructures and performing basic studies at the laboratory scale. The growth rate achieved by PLD can be varied from subangstrom per second to a few micrometers per hour by adjusting the repetition rate and the laser fluence, which is useful for both atomic

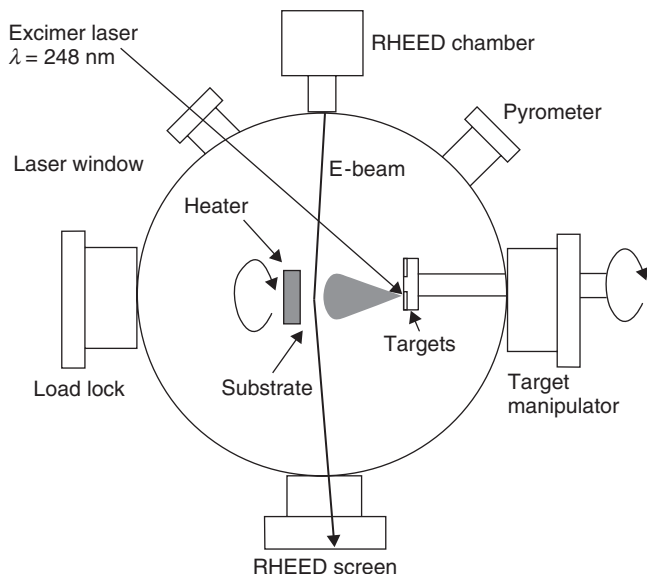


FIGURE 1.17 A sketch of the basic configuration of the pulsed laser deposition chamber (after Huang and Harris).

level investigations and thick layer growth. Moreover, the strong nonequilibrium growth conditions of PLD may allow a much broader range of metastable materials to be grown, including the introduction of higher dopant concentrations and alloy compositions that in equilibrium phase normally segregate.

There are three main stages of the PLD process: laser–target interaction, laser–plume interaction, and subsequent deposition of the thin film. In the beginning of the laser pulse, the optical energy is largely absorbed by the surface of the target. Since the laser energy is supplied to a small volume of 10^{-13} m^3 in a short time (typically 30 ns), the local temperature of the target, frequently on the order of 10^4 K . Therefore, all the species of the target evaporate simultaneously, that is, congruent evaporation. This condition ensures that the ejected materials have the same stoichiometry as the target which makes the PLD process particularly suitable for exploring binary, ternary, and more complicated systems without having to adjust fluxes from multiple sources. Continuous interaction of the laser beam with the plume results in the photodissociation and photoionization of the evaporated material. This interaction breaks molecular species and clusters and ionizes the evaporated material by nonresonant multiphoton process, leading to the formation of expanding plasma above the target surface, and transport toward the substrate.

The evaporation of the materials from targets by laser irradiation depends on the laser parameters (such as laser fluence, pulse duration, and wavelength) and material properties (such as reflectivity, absorption coefficient, and thermal

conductivity). According to Fig. 1.17a KrF excimer laser operating at a wavelength of 248 nm and pulse duration of 20 ns are used to ablate materials from the targets. The laser is incident at 45° from the target normal, and the substrate is centered along the target normal. The system is capable of holding six targets for multilayer growth. Each target is rotated about its axis to ensure uniform wear on the targets, and individual targets can be successively clocked into the position for the ablation of multitargets. A load lock chamber with a magnetically coupled transfer rod is equipped to facilitate the transfer of both targets and substrates without breaking the vacuum of main chamber. The base pressure, on the order of 10^{-8} torr, is achieved by pumping the chamber with turbo and mechanical pumps. The target to substrate distance can be varied over 15 cm to operate in different pressure regions. The substrate is rotated to enhance the temperature and thickness uniformity during deposition. The substrate heater is capable of reaching 800°C in either an oxygen ambient for oxide growth or a nitrogen ambient for nitride growth. Another attractive feature of PLD apparatus is the capability of *in situ* monitoring of the growth process, such as the reflection high energy electron diffraction (RHEED). The RHEED patterns offer abundant information on the crystal structure and the quality of the growing film. It also provides means to study surface structure and growth kinetics.

1.3.5 Molecular Beam Epitaxy Growth Technique

Despite the high price tag on the MBE reactor, it is one of the most versatile and widely used nonequilibrium growth techniques. While the MBE growth processes are under continuous development ranging from effusion cell shape to the addition of many *in situ* diagnostic tools, it has been used to grow almost any kind of doped and undoped semiconductor materials ranging from thin films and quantum wells to quantum dots and nanomaterials. It is capable of controlling the deposition of a submonolayer on substrates with various crystallographic structures. A schematic of an MBE growth chamber is shown in Fig. 1.18, which is showing the sources for the growth of GaAs and GaN with two different dopants (Si and Mg).

A thin film deposition process is performed inside the MBE chamber in which thermal beams of atoms or molecules react on the clean surface of a single-crystalline substrate that is held at high temperatures under ultrahigh vacuum conditions ($\sim 10^{-10}$ – 10^{-11} Torr) to form an epitaxial film. It turns out that this ultrahigh vacuum is a major advantage to the MBE growth. This is primarily due to this very low impurity environment and the fact that many *in situ* tools can be added to the vacuum chamber. The most common way to create molecular beam for MBE growth is through the use of Knudsen effusion cells. The crucibles employed in Knudsen cells are mostly made of PBN. The temperatures of different crucibles are usually independently controlled to within $\pm 1^\circ\text{C}$.

The material sources could be solid, gas, or metal–organic materials. Solid precursor sources are generally solids that are heated above their melting point in effusion cells, Knudsen cells. The atoms of source material escape the cell

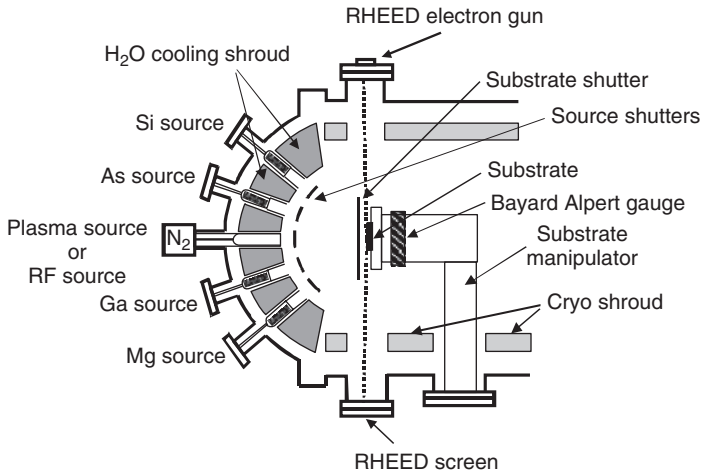


FIGURE 1.18 A sketch of a molecular beam epitaxy growth chamber showing the configuration of the sources and RHEED electron guns.

into the vacuum chamber by thermoionic emission. The beam flux is a function of its vapor pressure, which can be controlled by the source temperature. In the gas source MBE, group V of III–V semiconductors are connected through an injector or cracker. The gas source beam flux is controlled by using a mass flow controller. The metal–organic sources are either liquids or powders. An inert carrier gas is usually used to control the beam flux. The thickness and compositions of the epitaxial layers are controlled by the interruption of the unwanted atomic beam using shutters, which are usually remotely controlled by a computer. The beam of atoms and molecules will attach to the substrate forming the epitaxial layers. The growth rate is generally about a monolayer per second. The layers crystallize through the reaction between the atomic or molecular beams of the source materials and the substrate surface that is maintained at a certain temperature.

Another major difference between the MBE growth and other growth techniques is that it is far from thermodynamic equilibrium conditions. It is mainly governed by the kinetics of the surface processes. The five major kinetic processes are illustrated in Fig. 1.19 where the blocks represent the atoms and molecules that reach the surface of the substrate. Process (a) is the adsorption of the atoms or molecules impinging on the substrate surface; process (b) is the thermal desorption of the atoms or molecules that are not incorporated in the epitaxial layer; process (c) is the surface migration and dissociation of the absorbed atoms and molecules; process (d) is the incorporation of the atoms and molecules into the epitaxial layer or the surface of the substrate; and process (e) is the interdiffusion between the substrate and the epitaxial layer.

In order to grow smooth surfaces, the atoms impinging on the substrate surface should be given enough time to reach their proper position at the edge before

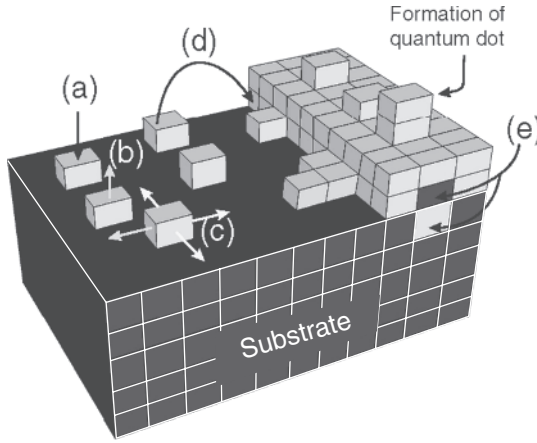


FIGURE 1.19 A schematic illustration of the kinetic processes that occur at the surface of the substrate during the MBE growth.

the formation of the next entire new layer. This also reduces the formation of defects and dislocations. The atoms in the MBE growth chamber have a long mean-free path where collisions and scattering with other atoms are infrequent before reaching the surface of the substrate. This mean-free path, \mathcal{L} , can be written in terms of the atoms or molecules concentration, \mathcal{N} , according to the following relation

$$\mathcal{L} = \frac{1}{\sqrt{2}\pi\mathcal{N}d^2}, \quad (1.32)$$

where d is the diameter of the species. The concentration, \mathcal{N} , is determined by the vapor pressure, P , and temperature, T , inside the MBE chamber according to the following relation

$$\mathcal{N} = \frac{P}{k_{\text{B}}T}, \quad (1.33)$$

where k_{B} is the Boltzmann constant.

As mentioned earlier, one of the advantages of having an ultrahigh vacuum in the MBE growth chamber is that *in situ* tools can be added to monitor the epitaxial layer during growth. One of these tools is the reflection high energy electron diffraction abbreviated or known as *RHEED*. The electron energy in the RHEED gun is typically 5–50 keV. The electrons are directed toward the substrate at a grazing angle $\theta \leq 1$. A schematic showing the RHEED configuration is shown in Fig. 1.20a. The electrons are then diffracted by the epitaxial layer formed at the substrate surface. This leads to the appearance of intensity-modulated streaks on a fluorescence screen. The results obtained by RHEEDS are generally characterized as static or dynamic mode. In the static mode, the atomic construction of the surface can be determined from RHEED diffraction patterns. These patterns (Fig. 1.20b) usually provide information on the atomic

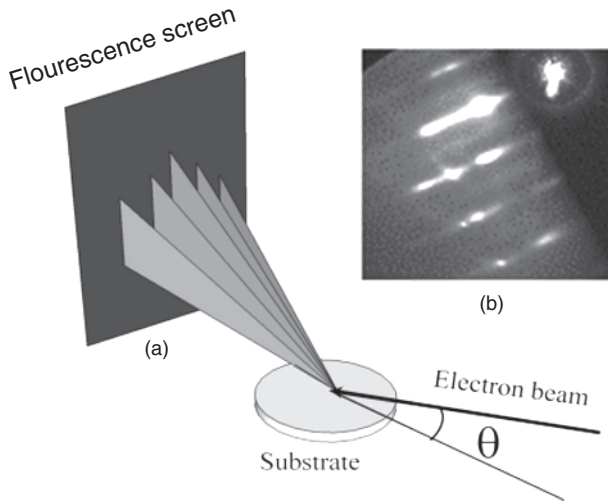


FIGURE 1.20 (a) The configuration of the RHEED inside the MBE chamber, and (b) RHEED patterns formed on a fluorescence screen.

surface construction, which is a function of the incoming electron beam flux, the substrate temperature, and the strain of the epitaxial layer. On the other hand, the dynamic mode is based on the change of the intensity of the central diffraction streak as the wafer roughness changes over time. This process is illustrated in Fig. 1.21, where the formation of a single complete monolayer is shown. The fractional layer coverage is represented by the factor S . During the epitaxial growth process, the roughness of the epitaxial layer increases as a new atomic layer forms. When the surface coverage reaches 50% or $S = 0.5$, the roughness is at maximum and begins to decrease as the growing layer is complete, which corresponds to minimum roughness ($S = 1.0$). The intensity of the main RHEED streak follows the period oscillation of the layers roughness with the maximum intensity corresponding to the minimum roughness. This is illustrated in the RHEED oscillation signal depicted in the right-hand side panel. The time separation between the two adjacent peaks in the RHEED oscillations provides the time needed for the growth of a single layer of a crystal.

Another *in situ* tool that is often used in MBE growth chamber is Auger electron spectroscopy. This technique is based on the Auger effect of measuring the elemental composition surface. This technique uses an electron beam with energy ranging between 3 and 25 keV which when hits the substrate surface, it excites the atoms at the surface of the substrate by knocking a core level electron to a higher energy level. When the excited electrons relax, the atoms release the extra energy by emitting Auger electrons with characteristic energies. These energies are measured, and the quantity of Auger electrons is proportional to the concentration of the atoms on the substrate surface. Thus, Auger electron spectroscopy technique measures the planar distribution of elements on a surface.

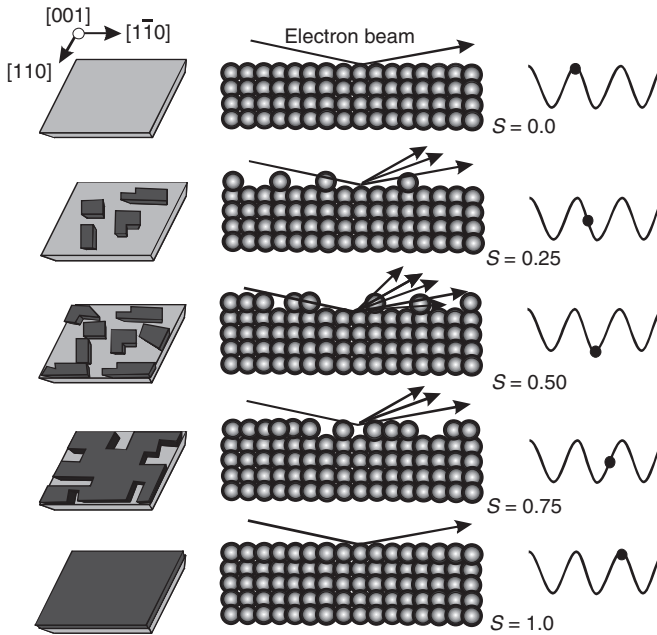


FIGURE 1.21 An illustration of the formation of a single monolayer as seen by an RHEED *in situ* instrument. The corresponding RHEED oscillation signal is shown.

This technique can also be used to measure the depth profile when used in conjunction with an ion sputtering method.

1.3.5.1 Example of a Molecular Beam Epitaxy Growth: III-Nitrides The growth of many semiconductor material thin films and quantum structures by MBE technique, in particular III–V semiconductors, is approaching maturity in almost every aspect. Recently, this technique has been employed in growing GaN and related compounds. The MBE sketch shown in Fig. 1.17 is in fact configured to grow GaN structures. One of the major issues in the deposition of GaN and group III-nitrides by MBE is the incorporation of an appropriate nitrogen source, since molecular nitrogen (N_2) does not chemisorb on Ga because of its large binding energy of 9.5 eV. To solve this problem, different approaches are currently being reported for the growth of cubic and hexagonal group III-nitrides. The first approach is the use of gaseous sources such as ammonia (NH_3) or dimethylhydrazine (DMH), this kind of MBE is also called *chemical beam epitaxy* (CBE) or *reactive ion molecular beam epitaxy* (RMBE). This compound is quite thermally stable and as a result limits the growth temperature significantly. Therefore, lower growth temperatures, such as those needed for low temperature nucleation buffers or for layers containing indium, cannot be grown as easily with NH_3 . DMH has higher reactivity than NH_3 and is expected to produce better quality crystals.

The second approach utilizes plasma-activated molecular nitrogen supplied via DC plasma sources, microwave plasma-assisted electron cyclotron resonance (ECR) plasma sources, or RF plasma sources. However, because of the low growth rate of 10–30 nm/h, imposed by the limited nitrogen flux of the DC source, the synthesis of a 1 μm thick film would require approximately 50 h, making it almost impossible to achieve stable growth conditions throughout such a run. ECR sources rely on coupling microwave energy at 2.45 GHz with the resonance frequency of electrons in a static magnetic field. Such coupling allows for ignition of the plasma at low pressures and powers and produces a high concentration of radicals. In an ECR source, approximately 10% of the molecular nitrogen is converted into atomic nitrogen. Because these sources operate very efficiently at fairly low powers, they are usually cooled by air. A typical growth rate of an ECR source is about 200 nm/h. A detailed description of the design and principle of operation of microwave plasma-assisted ECR sources is given by Moustaka. The physical properties of binary nitrides, namely GaN, AlN, and InN, are tabulated in Table 1.1.

Nitrogen plasmas are generated by inductively coupling RF energy at a frequency of 13.56 MHz into a discharge chamber filled with nitrogen at pressures of $>10^{-6}$ mbar. The discharge tube and the beam exit plate can be fabricated from pyrolytic boron nitride (BN) avoiding quartz, which may be a source of residual Si or O doping of GaN. The plasma sheath effect confines ions and electrons within the plasma discharge regions allowing only low energy (<10 eV) neutral species to escape. Therefore, these sources are believed to produce significant concentration of atomic nitrogen. Owing to the very high powers used

TABLE 1.1 A List of Physical Parameters of GaN, AlN, and InN

Parameter	Notation	Unit	GaN	AlN	InN
Lattice constant	a	\AA	3.189	3.112	3.548
Lattice constant	c	\AA	5.185	4.982	5.760
Thermal coefficient	$\Delta a/a$	10^{-6} K^{-1}	5.59	4.2	—
Thermal coefficient	$\Delta c/c$	10^{-6} K^{-1}	3.17	5.3	—
Band gap, 300 K	E_g	eV	3.42	6.2	0.68
Band gap, 4 K	E_g	eV	3.505	6.28	—
Electron effective mass	m_e	m_0	0.22	—	—
Hole effective mass	m_h	m_0	>0.8	—	—
Elastic constant	C_{13}	GPa	94	127	100
Elastic constant	C_{33}	GPa	390	382	392
Static dielectric Constant	ϵ_r	ϵ_0	10.4	8.5	15.3
Spontaneous polarization	P_{spn}	C/m^2	-0.029	-0.081	-0.032
Piezoelectric coefficient	e_{31}	C/m^2	-0.49	-0.60	-0.57
Piezoelectric coefficient	e_{33}	C/m^2	0.73	1.46	0.97
Binding energy, exciton A	E_{xb}	meV	21	—	—
Thermal conductivity	κ	W/cm.K	2.1	2.85	—
Refractive index	n_r	—	2.2	2.15	—
Melting point	T_m	K	>2573	>3000	—

in these sources, up to 600 W, the plasma chambers are usually water cooled. RF sources permit growth rates up to about 1 $\mu\text{m/h}$.

All epitaxial growth requires bulk substrates. Bulk GaN is difficult to grow since high pressure and high temperature growth conditions are required (see Manasreh and Ferguson). Thus, substrates other than GaN are currently being used for the growth of epitaxial GaN thin films, heterojunctions, and quantum wells. The most common used substrates are sapphire (Al_2O_3) and SiC. The properties of these substrates are listed in Table 1.2. Although sapphire has a rhombohedral structure, it can be described by a hexagonal material. The hexagonal structure of sapphire provides the same orientation of the grown GaN layer of wurtzite

TABLE 1.2 A List of Physical Parameters of Sapphire and SiC

Parameter	Sapphire	SiC
Lattice constant (nm)		
$a = 0.4765 @20^\circ\text{C}$	3C	$a = 0.43596$
$c = 1.2982 @20^\circ\text{C}$	2H	$a = 0.30753, c = 0.50480$
	4H	$a = 0.30730, c = 1.0053$
	6H	$a = 0.30806, c = 1.51173$ (Harris)
Melting point ($^\circ\text{C}$) 2030	3C	2793 (Weast <i>et al.</i>)
Density (g/cm^3) 3.98 @20 $^\circ\text{C}$	3C	3.166
	2H	3.214
	6H	3.211 (Harris)
Thermal expansion coefficients (10^{-6}K^{-1})		
6.66 to c -axis @20–50 $^\circ\text{C}$	3C	3.9
9.03 to c -axis @20–10 ^{30}C	4H	4.46 a -axis
5.0 \perp to c -axis @20–10 ^{30}C		4.16 c -axis (Ambacher)
% change in lattice constants between 293–1300 K for Al_2O_3 and 300–1400 K for SiC		
$a/a_0 = 0.83$	6H	$\Delta a/a_0 : 0.4781$ $\Delta c/c_0 : 0.4976$
$c/c_0 = 0.892$	3C	$\Delta a/a_0 : 0.5140$ (Reeber <i>et al.</i>)
Thermal conductivity ($\text{W/cm}\cdot\text{K}$)		
0.23 to c -axis @296 K	3C	3.2
0.25 to a -axis @299 K	4H	3.7
	6H	3.8 (Harris)
Heat capacity ($\text{J/K}\cdot\text{mol}$)		
77.9 @298 K	6H	0.71 (Harris)
Dielectric constants 8.6 to c -axis @10 2 –10 8 Hz	3C	$\epsilon(0):9.75$ $\epsilon(\infty):6.52$ (Harris)
10.55 to a -axis @10 2 –10 8 Hz	6H	$\epsilon(0):9.66, \epsilon(\infty) :6.52 \perp c$ -axis
		$\epsilon(0):10.3, \epsilon(\infty) :6.70 \parallel c$ -axis
Refractive index 1.77 @ $\lambda = 577$ nm	3C	2.6916 @ $\lambda = 498$ nm
1.73 @ $\lambda = 2.33\mu\text{m}$	2H	2.6686 @ $\lambda = 500$ nm
	4H	2.6980 @ $\lambda = 498$ nm
	6H	2.6894 @ $\lambda = 498$ nm (Harris)
Resistivity ($\Omega\cdot\text{cm}$) $> 10^{11}$ @300 K	4H	10^2 – 10^3 (Siergiej)
Young's modulus (GPa)		
452–460 in [0001] direction	3C	~ 440 (Harris)
352–484 in the [11 $\bar{2}$ 0] direction		

The parameters of sapphire were obtained from Belyaev.

symmetry. The growth of GaN on sapphire suffers from the lattice mismatch of interatomic separation in the (0001) interface and from the mismatch of thermal expansion coefficients. The large lattice constant mismatch between GaN and sapphire causes the film to be completely relaxed (not strained). This large lattice constant mismatch must be improved by introducing various processing scheme, such as surface preparation, substrate nitridation, and the growth of buffer layers.

Surface Preparation: Wet and *in situ* methods of etching sapphire include phosphoric acid (H_3PO_4), sulfuric–phosphoric acid mixtures, H_2SO_4 – H_3PO_4 fluorinated and chlorofluorinated hydrocarbons, tetrafluoro sulfur (SF_4), and sulfur hexafluoride (SF_6). However, the most common substrate preparation procedure before the growth of GaN is to simply heat the sapphire under flowing hydrogen at high temperatures.

Sapphire Nitridation: Sapphire is nitridated by exposure to nitrogen plasmas or thermally cracked ammonia in MBE systems. Under the conditions of temperature used for MBE growth, $\text{AlO}_x\text{N}_{1-x}$ should be unstable and nitridation of sapphire results in the formation of AlN. The AlN layer promotes GaN nucleation and increases the wetting of the GaN over layer from 550 to 820°C in MBE growth. The benefits of the nitridation layer are due to a change in the surface energy in the low temperature GaN or AlN buffer layer. The nitridation of sapphire before the growth of a low temperature buffer AlN or GaN is an important step for reducing the defect density, enhancing the electron mobility, and reducing the yellow luminescence in subsequently deposited films. The chemical alternation of surfaces of sapphire substrates using particle beams can be used as an alternative process to nitridation. The advantage of this method over nitridation is its simplicity and room temperature operation. The reactive ion (N_2^+) beam has also been used for pretreatment of sapphire substrates.

Buffer Layer: A low temperature (LT) GaN or AlN buffer (the growth temperature is usually about 400°C for MBE) is an important technique for III-nitride growth, since it can dramatically improve the surface morphology and crystalline quality of GaN sequentially deposited at high temperature (700–850°C for MBE growth).

Polarity: Control of polarity of GaN film is critical in epitaxial growth. This is because it will change surface morphology, doping characteristics, and most importantly, it will determine the direction of piezoelectric field, which is crucial to the device performance.

Other Substrates: In addition to sapphire substrate, III-nitride materials have been grown on other substrates such as SiC, GaAs, and Si (for more details, see Liu and Edgar). The SiC substrates are second to sapphire for epitaxial growth of GaN thin films and quantum structures. The most common polytype SiC structures are illustrated in Fig. 1.22. It has several advantages over sapphire including a smaller lattice constant mismatch (3.1%) for [0001] oriented films, a much higher thermal conductivity (3.8

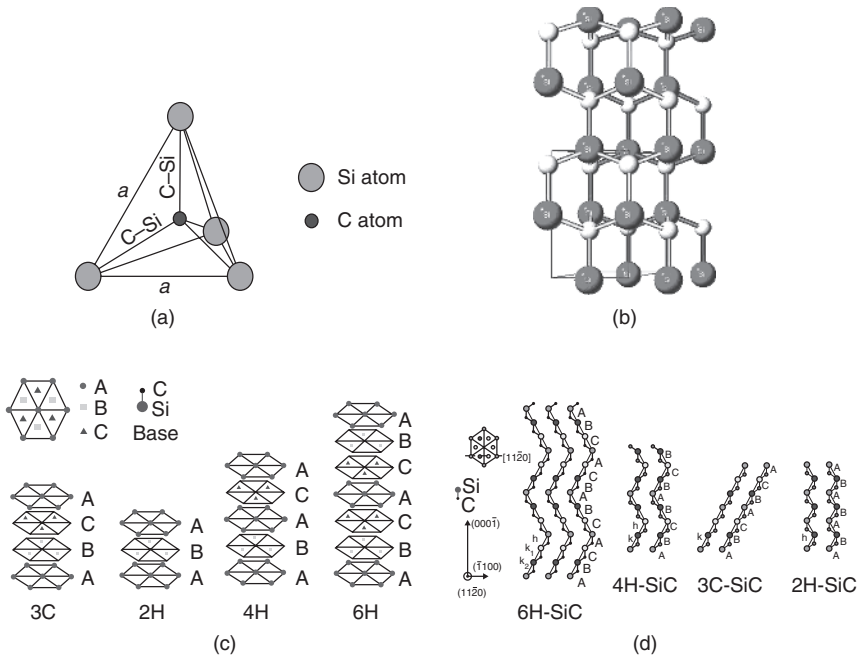


FIGURE 1.22 (a) The tetragonal bonding of a carbon atom with the four nearest silicon neighbors. The distance a and C–Si bond are approximately 3.08 and 1.89 Å, respectively, (b) the three-dimensional structure of 2H-SiC structure, (c) the stacking sequence of double layers of the four most common SiC polytypes, and (d) the $[11\bar{2}0]$ plane of the 6H-, 4H-, 3C-, and 2H-SiC polytypes (after Gith and Pentusky).

$\text{Wcm}^{-1} \text{K}^{-1}$), and low resistivity, so electrical contacts to the backside of the substrate are possible.

The lattice constant mismatch for SiC is smaller than that of sapphire, but it is still sufficiently large to cause a large density of defects to form in the GaN layers. The crystal planes in epitaxial GaN parallel those of the SiC substrate, making facets for lasers easier to form by cleaving. It is available with both carbon and silicon polarities, potentially making control of the GaN film polarity easier. High gain heterojunction bipolar transistors taking advantage of the discontinuity created at the GaN–SiC interface are possible. However, SiC does have its disadvantages. Gallium nitride epitaxy directly on SiC is problematic, because of poor wetting between these materials. This can be remedied by using an AlN or $\text{Al}_x\text{Ga}_{1-x}\text{N}$ buffer layer but at the cost of increasing the device resistance. This roughness and also remnant subsurface polishing damage are sources of defects in the GaN epitaxial layer. The screw dislocation density in SiC is $10^3\text{--}10^4 \text{ cm}^{-2}$, and these defects may also propagate into the GaN epitaxial layer and/or degrade device performance. The thermal expansion coefficient of SiC is less than

that of AlN or GaN; thus, the films are typically under biaxial tension at room temperature. Finally, the cost of silicon carbide substrates is high.

Silicon Substrate: Silicon substrates possess physical properties, including high quality and low cost, that are very attractive to GaN-based devices. The physical parameters of bulk silicon are listed along those of GaAs in Table 1.3. The crystallographic structure of silicon is shown in Fig. 1.12. Silicon wafers are very low priced and are available in very large sizes because of its mature development and large-scale production. Silicon has good thermal stability under GaN epitaxial growth conditions. The crystal perfection of silicon is better than any other substrate material used for GaN epitaxy, and its surfaces can be prepared with extremely smooth finishes. The possibility of integrating optoelectronic GaN devices with Si electronic devices is another advantage. To date, the quality of GaN epitaxial layers on silicon has been much poorer than that on sapphire or silicon carbide, because of a large lattice constant and thermal expansion coefficient mismatch, and the tendency of silicon to form an amorphous silicon nitride layer when exposed to reactive nitrogen sources. Gallium nitride and AlN grown on Si(111) are highly defective and nonradiative carrier recombination channels severely limit the luminescence efficiency for device application.

GaAs Substrate: The crystallographic structure of GaAs is zincblende, which is shown in Fig. 1.13. Gallium nitride materials have been grown on zincblende GaAs (for more details on the subject, see As), which is most widely used III–V compound semiconductor as a substrate for zincblende GaN epitaxy since it is well developed and large area substrates are commercially available. The properties of GaAs are listed in Table 1.3. In principle, zincblende structures of GaN possess superior electronic properties for device applications, such as a higher mobility, isotropic properties

TABLE 1.3 Physical Parameters of Silicon and GaAs

Properties	Silicon	GaAs
Lattice constant (nm)	0.543102	0.56536
Density (g/cm ³)	2.3290	5.32
Melting point (°C)	1410	1240
Heat capacity (J/g·K)	0.70	0.327
Thermal conductivity (Wcm·K)	1.56	0.45
Thermal diffusivity (cm ² /s)	0.86	0.26
Thermal expansion(linear) × 10 ⁻⁶ K ⁻¹	2.616	6.03
% change in lattice (298K~ 1311K)	$\Delta a/a_0$: 0.3995	$\Delta a/a_0$: 0.5876
Bulk modulus (GPa)	97.74	75.0
Young's modulus (GPa)	165.6	85.5
Refractive index	3.42	3.66
Dielectric constant	11.8	13.1

because of the cubic symmetry and high optical gain. These advantages may not have been realized due to the difficulty in producing low defect content material. The growth of zincblende GaN requires (001)-oriented substrates having fourfold symmetry. Several substrates, such as GaAs, Si, 3C-SiC, GaP, and MgO, can be used to grow zincblende GaN. The isoelectronic structure (i.e., both GaAs and GaN are III–V compounds), shared element (Ga), potential to convert the surface of GaAs to GaN, and cleavage planes parallel to the epitaxial GaN cleavage planes are the major material advantages of GaAs as a substrate for GaN epitaxy. Technological advantages include a well-established process technology, several readily available substrate orientations of both polar and nonpolar varieties, and low resistance ohmic contacts. There are several disadvantages to GaAs substrates, including a large lattice constant and thermal expansion coefficient mismatch, a poor thermal conductivity, and perhaps most problematic, low thermal stability.

GaAs is much more readily wet etched than sapphire, making GaN films easier to separate from GaAs than sapphire. Thus, GaAs(111) substrates are considered a better template for creating free-standing thick GaN films for subsequent epitaxy and device fabrication, with the ultimate goal of eliminating the problems associated with heteroepitaxy. Since the decomposition rate of GaAs in N_2H_4 or an ultrahigh vacuum rapidly increases at temperatures above 700°C , this imposes limits on the epitaxial growth temperature of GaN and hence its maximum growth rate. Even a small amount of GaAs decomposition is detrimental to zincblende GaN epitaxy, as surface roughening or faceting enhances the onset of wurtzite growth. Since MBE is capable of depositing epitaxial GaN films at a lower temperature, it has been more commonly employed than MOCVD or HVPE when GaAs is the substrate.

1.3.5.2 Growth Rate The gas impingement flux, Φ , on the surface of a substrate is a measure of the frequency with which atoms and molecules impinge on, or collide with, the surface. This flux can be defined in one dimension as the number of molecules or atoms striking a surface per unit area and unit time, assume that the surface is perpendicular to the direction of the atoms or molecules motion, which can be expressed as (see Ohring)

$$\Phi = \int_0^{\infty} v_x d\mathcal{N}_x, \quad (1.34)$$

where

$$d\mathcal{N}_x = \mathcal{N}f(v_x)dv_x, \quad (1.35)$$

$f(v_x)$ is the velocity distribution function described by a Maxwell–Boltzmann form as

$$f(v_x) = \sqrt{\frac{M}{2\pi RT}} e^{-\frac{Mv_x^2}{2RT}}, \quad (1.36)$$

M is the atomic or molecular weight, R is the gas constant, T is temperature, and v_x is the velocity of the atoms or molecules. By combining Equations 1.34–1.36, the flux is obtained as

$$\Phi = \mathcal{N} \sqrt{\frac{M}{2\pi RT}} \int_0^{\infty} v_x e^{-\frac{Mv_x^2}{2RT}} dv_x = \mathcal{N} \sqrt{\frac{M}{2\pi RT}} \frac{RT}{M} = \mathcal{N} \sqrt{\frac{RT}{2\pi M}}. \quad (1.37)$$

Substituting the ideal gas equation, $P = \mathcal{N}RT/N_A$, into Equation (1.37) yields

$$\Phi = \frac{PN_A}{\sqrt{2\pi MRT}} \approx 3.513 \times 10^{22} \frac{P}{\sqrt{MT}} \text{ molecules}/(\text{cm}^2/\text{s}), \quad (1.38)$$

where P is the gas vapor pressure in Torr. Consider a gas escaping a container through an opening of an area \mathcal{A} into a region where the gas concentration is zero. Thus, the rate at which the molecules leave the container is $\Phi\mathcal{A}$ and the corresponding volume flow per second is $\dot{V} = \Phi\mathcal{A}/\mathcal{N}(\text{cm}^3\text{sec}^{-1})$, which can be rewritten as $\dot{V} = 3.64 \times 10^3 \sqrt{T/M} \mathcal{A} \text{cm}^3 \cdot \text{sec}^{-1}$.

Another aspect of the gas impingement flux is to calculate the time required for a surface to be coated with one monolayer of gas molecules. The characteristic deposition time, \mathcal{T} , is inversely proportional to the impingement flux. It is the ratio between the surface density and the impingement flux. The surface density of most semiconductor crystals is on the order of $\sim 7 \times 10^{14}$ atoms/cm². Thus, \mathcal{T} can be obtained as

$$\mathcal{T} = \frac{7 \times 10^{14} \text{ atoms}/\text{cm}^2}{\Phi} = \frac{7 \times 10^{14} \sqrt{MT}}{3.513 \times 10^{22} P} \approx 2.0 \times 10^{-8} \frac{\sqrt{MT}}{P} \text{ sec}. \quad (1.39)$$

The pressure is measured in Torr. For a gas with an atomic weight of 30 g/mole, the deposition time at $T = 300$ K in 1 Torr pressure is $\sim 1.9 \times 10^{-6}$ sec. On the other hand, if the pressure is 10^{-10} Torr, then the deposition time is ~ 5.3 h.

Now, let us consider a substrate positioned at a distance l from an aperture of an area \mathcal{A} of a source in an MBE growth chamber. The number of molecules, \mathcal{M} , striking the substrate per unit area per second can be expressed as (see Cho)

$$\mathcal{M} = 3.513 \times 10^{22} \frac{P\mathcal{A}}{\pi l^2 \sqrt{MT}} \text{ molecules}/(\text{cm}^2/\text{s}). \quad (1.40)$$

For a Ga source in a BN crucible with an opening of $\mathcal{A} = 10$ cm² and $l = 20$ cm, the deposition rate can be calculated as follows: assume the source temperature is 970°C or 1243 K and the vapor pressure is 1×10^{-4} Torr. With an atomic weight of 70 g/mole, the arrival rate of Ga atoms at the substrate can be calculated from (1.40) as $\sim 9.5 \times 10^{13}$ atoms/(cm².sec). The average GaAs monolayer thickness is 2.83 Å and contains $\sim 6.3 \times 10^{14}$ Ga atoms/cm². Hence, the growth rate is $[(9.5 \times 10^{13})/(6.3 \times 10^{14})] \times 2.83 \times 60 \simeq 25.5$ Å/min.

The layer thickness can also be measured using the optical interference method. Consider Fig. 1.23 where the incident light reaches the thin film at an angle. Part of the light will be transmitted through the thin film and the substrate, but a portion of the light will be reflected back and forth between the two interfaces of the thin film. As the photons are bounced between the interfaces, the intensity of the light decreases and an interference pattern is formed due to the difference in the phase of the electromagnetic wave. If the m^{th} order maximum occurs at wavelength λ_1 and the $(m+1)^{\text{th}}$ order occurs at λ_2 , we have

$$2n_r d \cos \theta = m\lambda_1 = (m + 1)\lambda_2, \tag{1.41}$$

where d is the thickness of the layer, n_r is the refractive index of the layer material, and θ is the diffraction angle inside the layer. Equation (1.41) can be

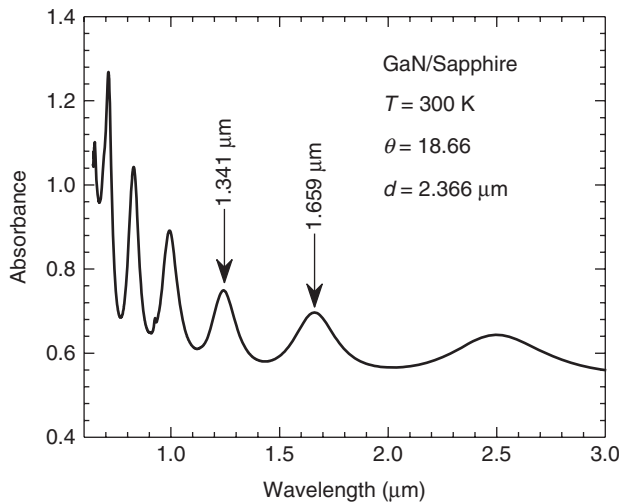
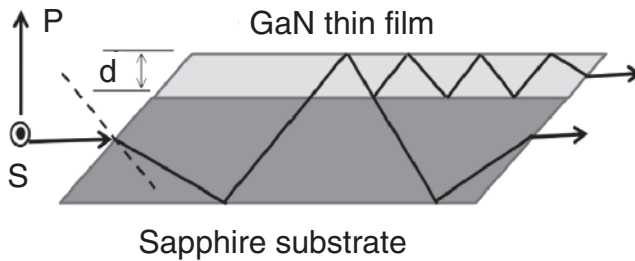


FIGURE 1.23 (a) Waveguide configuration of GaN thin film on a sapphire substrate with an internal diffraction angle of 18.66° . (b) An optical interference pattern in a thin layer is illustrated as the electromagnetic wave bounce back and forth between the two layer interfaces.

rewritten in a more general form as

$$d = \frac{N_f}{2n_r \left(\frac{1}{\lambda_2} - \frac{1}{\lambda_1} \right) \cos \theta}, \quad (1.42)$$

where N_f is the number of fringes between λ_1 and λ_2 . The separation between the fringes decreases as the layer thickness is increased. The lower panel in Fig. 1.23 is an actual interference pattern observed in a GaN thin film grown by MOCVD on sapphire. By choosing any two adjacent peaks, the thickness can be calculated by using Equation (1.42). For normal incident light, θ is zero and $\cos \theta$ is 1. The diffraction internal angle is calculated to be 18.66° for the waveguide configuration shown in Fig. 1.23a.

Experimentally, the actual growth rate of thin films is determined by the measured layer thickness divided by the growth time. Finally, the mole fraction, x , of a ternary compound $A_xB_{1-x}C$ can be determined from the growth rates as

$$x = \frac{\mathcal{G}(A_xB_{1-x}C) - \mathcal{G}(BC)}{\mathcal{G}(A_xB_{1-x}C)}. \quad (1.43)$$

For example, if the growth rates of $Al_xG_{1-x}As$ and GaAs are 36 and 25 Å, respectively, then $x = (36-25)/36 \sim 0.30$.

1.3.5.3 Metal-organic Chemical Vapor Deposition Growth Technique Metal-organic chemical vapor deposition (MOCVD) also known as *metal-organic vapor-phase epitaxy* (MOVPE) is becoming one of the most widely used techniques for the growth of various semiconductor films and structures. It is capable of mass production, where several wafers can be used at the same time for a single run. Thus, most industrial applications rely on this technique for mass production. For the growth of III-V semiconductor compounds, this technique relies on the pyrolysis of metal-organic compounds containing group III elements in an atmosphere of hydrides containing group V elements. Both the metal-organic compounds and the hydride gases are introduced in the reactor chamber in which a bulk semiconductor substrate is placed on a heated susceptor. The substrate has a catalyst effect on the decomposition of the gaseous products. The substrate temperature is usually higher than the temperature of the precursor sources. A sketch of the MOCVD reaction is shown in Fig. 1.24. The gas handling system includes the metal-organic sources, hydride sources, valves, pumps, and any other instruments needed to control the gas flows. The most common carrier gases in MOCVD reactors are hydrogen, nitrogen, argon, and helium.

The metalorganic compounds are either liquids or powders contained in stainless steel cylinder known as *bubblers*. The partial pressure of the source is regulated by controlling the temperature and total pressure inside the bubbler. Mass flow controllers are used to control the mass flow rate of hydride and carrier gases. By sending a controlled flow of carrier gas through the bubbler,

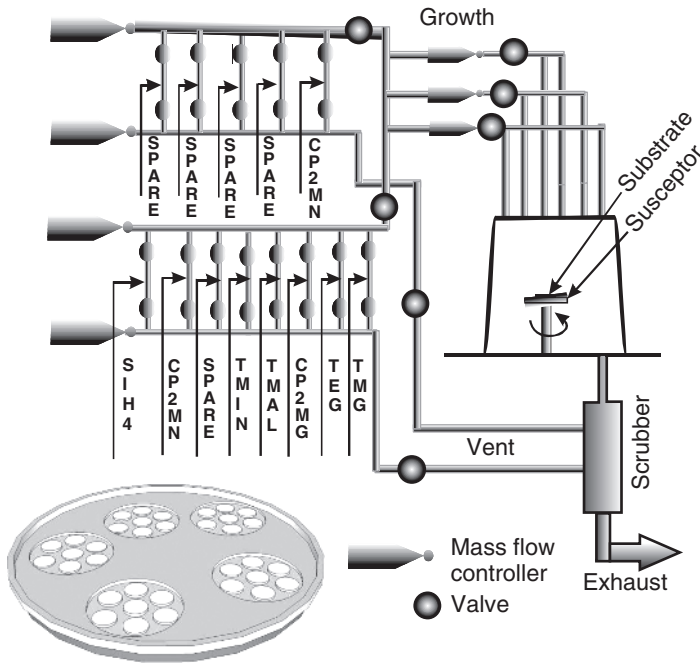


FIGURE 1.24 A sketch of an MOCVD reactor showing gas inputs with valves and mass flow controllers. The sketch in lower left corner is a sample holder with several wafers to illustrate the mass production capability of this growth technique.

the mass flow in a form of dilute vapors of the metal–organic compounds is obtained. The purity of the sources is of paramount importance in the growth of layered structures such as quantum wells and quantum dots. Thus, efforts are devoted to constantly purify source materials.

The reactor chamber is made of stainless steel containing the susceptor, which can hold one or several substrates as illustrated in Fig. 1.24. A commercial MOCVD reactor can hold many 2 in. wafers. The susceptor can be heated by different methods including RF induction heating, radiative heating (lamp), and resistance heating. Knowing and controlling the temperature of the substrate is extremely important for the growth of thin films and quantum structures. One of the recent schemes used to heat the substrate and control its temperature in MOCVD reactors is shown in Fig. 1.25.

In the MBE world, the substrate temperature is controlled by monitoring its band gap absorption edge as a function of temperature. In case of MOCVD, the temperature is basically controlled by measuring the wafer holder (Pocket) temperature as shown in Fig. 1.25. The schematic in Fig. 1.25a consists of LED, filter, photodiode, electronics, and software. An enlarged portion of the substrate is shown in Fig. 1.25b where the substrate temperature is actually the Pocket temperature. Pyrometers are used to measure the Pocket temperature. This technique

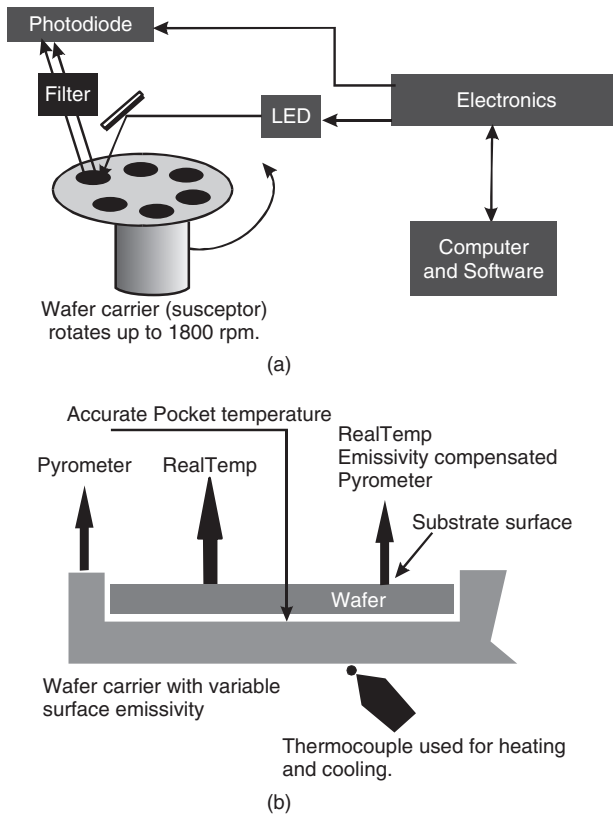


FIGURE 1.25 (a) A schematic of an *in situ* substrate temperature measurement is shown. (b) The substrate in the Pocket is enlarged as shown for clarity.

is actually the only method that one can use to measure the substrate temperature very accurately in case of transparent substrates such as sapphire, which is the commonly used substrate for the III-nitride heterostructures and nanostructures.

The band-gap of sapphire is over 7.3 eV (~ 170 nm) and the band gap measurement as a function of temperature is difficult to implement, since light sources in this spectral region are difficult to find and thermal radiance from the wafer surface is below the detection level. As the nitride materials are grown on the substrate, the emissivity from the deposited material can be measured. The basic idea is that the temperature of the substrate can be determined accurately and repeatedly by accurate wafer carrier Pocket temperature measurements. The thermocouple in Fig. 1.25b is used to give feedback to cooling and heating only, while the substrate temperature is measured by pyrometers as shown in the figure.

Two fundamental processes occur during the epitaxial growth. First, the thermodynamic process which determines the overall epitaxial growth. Second, the kinetic process which defines the growth rates. The thermodynamic calculations provide information about the solid composition of multicomponent materials

when vapor-phase compositions are known. The MOCVD growth is a nonequilibrium process, which cannot provide any information about the time required to reach equilibrium. It also cannot provide information about the transition from the initial input gases to the final semiconductor solid.

While the MOCVD growth technique has been used extensively in the epitaxial growth of materials, such as III-nitride compounds which require growth temperature over 1000°C , it has its own limitations. In particular, many *in situ* characterization tools, such as RHEED, scanning tunneling microscopy (STM), and Auger electron microscopy, cannot be used in the MOCVD chamber due to the fact that the MOCVD growth occurs at atmospheric pressure. However, other techniques, such as photoreflectance, ellipsometry, and optical transmissions, have been used recently during the MOCVD growth to monitor growth rates and thin film uniformity.

1.3.5.4 Chemical Vapor Deposition Technique The chemical vapor deposition (CVD) technique has many variations and is used to grow nanorods and nanotubes. A typical configuration is shown in Fig. 1.26. The general configuration of the growth apparatus is composed of a furnace, two quartz tubes, at least one mass flow controlled (MFC), gas cylinders, and a vacuum pump. In the case of ZnO nanorods growth, the zinc powder was placed on a wafer in the center of the furnace while several silicon or sapphire substrates with gold nanoparticles were lined up in the inner quartz tube as shown in the figure. This growth technique does not require specific substrates or crystallographic orientations. The gold nanoparticles are used as catalyst for the growth of the nanorods. The chamber is usually evacuated to about one milli-Torr and then flushed several times with nitrogen gas prior to the introduction of oxygen. The Zn powder temperature should be raised above the melting point of the Zn. A typical temperature ranges between 575 and 800°C depending on the desired nanorod size. The oxygen is introduced through the MFC with a rate of 10 sccm. Higher rates produced different nanorod sizes. The growth time ranges between 30 min and several hours. The nanomaterials grown on the substrate are usually removed from the furnace after cooling the system to room temperature. This technique produces all kind of nanomaterials with different shapes and orientations. An example of the material grown by this technique is shown in Fig. 1.27 for ZnO nanorods.

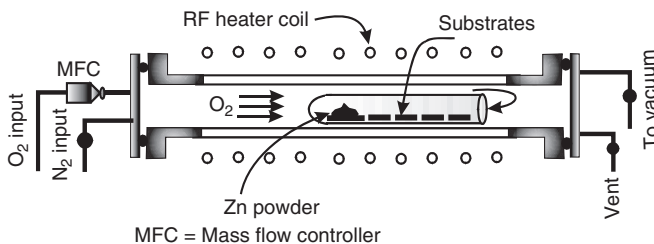


FIGURE 1.26 A sketch of the chemical vapor deposition furnace configuration. The growth of ZnO nanorods is taken as an example.

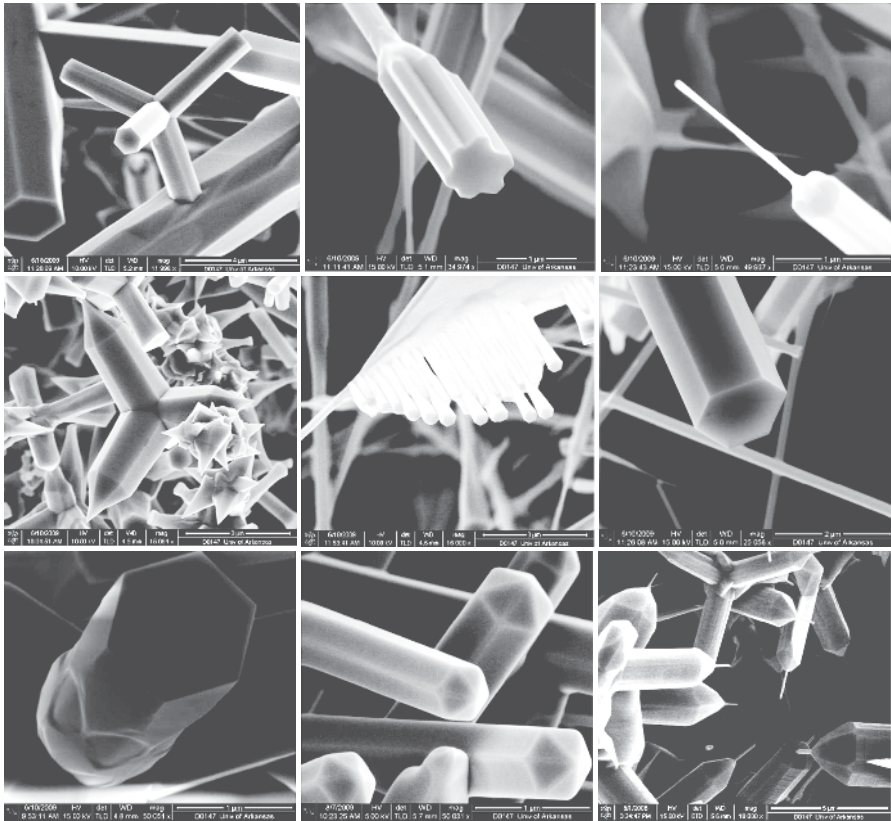


FIGURE 1.27 Several scanning electron microscope images of ZnO nanorods that were grown by the chemical vapor deposition technique. The shape and the size are due to the variation of the growth parameters.

The growth kinetics of CVD nanomaterials depends on a few factors associated with the heterogeneous reaction (gas–substrate interface), such as the transport of reactants through the boundary layer to the substrate, adsorption of reactant at the substrate, atomic and molecular surface diffusion, and transport of by-products away from the substrate through the boundary layer. While the microscopic details of these factors are difficult to model, the growth kinetics is often modeled in macroscopic terms and is capable of predicting the growth rate and uniformity of the grown materials. Following the discussion by Ohring, the reactor configuration is shown in Fig. 1.28. By assuming that the gas has a constant velocity component along the axis of the furnace tube, a constant temperature, and the reactor extends a large distance in the z -direction, the mass flux (\mathcal{J}) can be written as

$$\mathcal{J} = C(x, y)\bar{v} - D\nabla C(x, y), \quad (1.44)$$

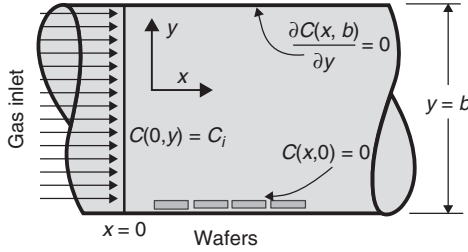


FIGURE 1.28 Horizontal reactor geometry used to obtain the growth rate.

where the first term represents a bulk viscous flow where the source of concentration $C(x,y)$ moving as a whole at a drift velocity \bar{v} . The second term represents the diffusion of individual gas molecules, with a diffusion coefficient D , along the concentration gradients. The flux source at the substrate surface is given by

$$\mathcal{J}(x) = D \frac{\partial C(x, y)}{\partial y} \Big|_{y=0} \quad \text{g/(cm}^2\text{s)} \tag{1.45}$$

where $C(x,y)$ is the solution of the steady-state continuity equation

$$D \left(\frac{\partial^2 C(x, y)}{\partial x^2} + \frac{\partial^2 C(x, y)}{\partial y^2} \right) - \bar{v} \frac{\partial C(x, y)}{\partial x} = 0, \tag{1.46}$$

and is given by

$$C(x, y) = \frac{4C_i}{\pi} \sin\left(\frac{\pi y}{2b}\right) e^{-\frac{\pi^2 D x}{4\bar{v} b^2}}. \tag{1.47}$$

where C_i and b are defined in Fig. 1.28. Equation (1.46) is subject to three conditions that are shown in figure, which are $C = 0$ for $y = 0$ and $x > 0$; $C = C_i$ for $x = 0$ and $b \geq y \geq 0$; and $\partial C/\partial y = 0$ for $y = b$ and $x \geq 0$. For an elemental semiconductor system, such as silicon (Si), the resultant deposition growth rate, \mathcal{G} , is related to $\mathcal{J}(x)$ according to the following relation

$$\mathcal{G} = \frac{m_{\text{Si}}}{\rho m_s} \mathcal{J}(x) \text{ cm/sec} \tag{1.48}$$

where m_{Si} and m_s are molecular weight of the silicon and the source gas, respectively. Combing Equations (1.45), (1.47), and (1.48) yields

$$\mathcal{G} = \frac{2C_i m_{\text{Si}}}{b \rho m_s} D e^{-\frac{\pi^2 D x}{4\bar{v} b^2}} \text{ cm/sec}. \tag{1.49}$$

This equation predicts an exponential decay of the growth rate as function of the distance along the reactor length, which is quite reasonable, since the input gases are progressively depleted of reactants. The expression of the growth rate provides design guidelines even though these guidelines are not always simple to implement.

1.4 FABRICATION AND GROWTH OF SEMICONDUCTOR NANOMATERIALS

Semiconductor nanomaterials have received significant attention in recent years. While the early techniques of producing these materials, such as quantum dots, relied on optical lithography, X-ray lithography, and electron beam lithography, the preferred method today is the epitaxial growth. The MBE, CVD, and MOCVD growth of nanomaterials is basically self-assembled growth. It is also possible to epitaxially grow nanomaterials on prepatterned substrates. Earlier production of quantum dots, for example, is made by lithography techniques with the multiple quantum wells as the starting materials. This production technique usually yields regular and uniform arrays of quantum dots where the charge carriers are confined in the three dimensions inside the dots.

During the early stages of epitaxial thin film formation, a small number of vapor atoms or molecules condense on the surface of the substrate. This stage is called *nucleation*. Modern *in situ* techniques such as STM and RHEED imaging provide useful information between the end of nucleation and the onset of nucleus growth. A nucleus here refers to as a collection of atoms that form the building block of the quantum dots. When the substrate is exposed to the incident vapor (atomic or molecular beams), a uniform distribution of small and highly mobile clusters or islands (three-dimensional structures or 3D) is observed. In this early growth stage, the prior nuclei incorporate impinging atoms to grow in size. As the growth continues, the islands merge together to form liquidlike materials especially at high substrate temperatures. Coalescence decreases the island density. Further deposition and coalescence causes the islands to connect forming unfilled channels. Additional deposition fills the channel and finally thin films are formed (two dimensional structures or 2D). The idea of the quantum dot growth is to form islands (3D structures) and discontinue the vapor depositions before a thin film (2D structure) is formed. The degree of confinement and the degree of freedom are illustrated in Table 1.4. One should distinguish between the degree of freedom and the degree of confinement. For example, 3D growth means three degree of confinement while the 0D degree of freedom means the charge carriers are confined by three directions, which indicates a quantum dot.

There are three well-known modes of heteroepitaxial growth, which are illustrated in Fig. 1.29. First, the island or Volmer-Weber mode, Fig. 1.29a, which is characterized by the island growth when the smallest stable clusters nucleate

TABLE 1.4 The Confinement and the Degree of Freedom for Bulk and Quantum Wells, Wires, and Dots

	Confinement	Degree of Freedom
Bulk	0D	3D
Quantum well	1D	2D
Quantum wire	2D	1D
Quantum dot	3D	0D

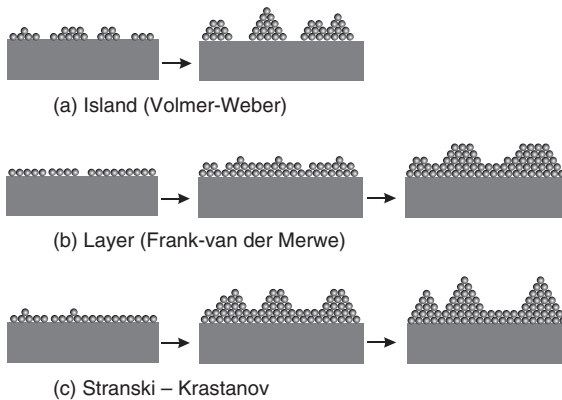


FIGURE 1.29 The three common growth modes of heteroepitaxy. (a) island or Volmer-Weber mode, (b) layer or Frank-van de Merwe mode, and (c) layer-island or Stranski–Krastanov mode.

on the substrate and grow in 3D to form islands (quantum dots). This mode occurs when the atoms or molecules in the deposit are more strongly bound to each other than to the substrate. An example of this growth mode is the deposition of metals on insulators. Second, the layer or Frank-van de Merwe mode as demonstrated in Fig. 1.29b, which is opposite to the island mode during the layer growth. The extension of the smallest stable clusters occurs primarily in two dimensions, resulting in the formation of planar film. The atoms in this mode are more strongly bound to the substrate than to each other. The first complete layer is then covered with a less tightly bound second layer. An example of this mode is the growth of single-crystal semiconductor thin films. Third, the Stranski–Krastanov (SK) mode shown in Fig. 1.29c, which is known as *layer plus island mode*, is an intermediate combination of both the island and layer modes. After forming one or two monolayers, subsequent layer growth becomes unfavorable and islands form. The layer composed of the first two or three monolayers formed at the surface of the substrate, or even the buffer layer, is often called “*wetting layer*.”

The transition from 2D to 3D growth is still not well understood. However, any effect that disturbs the monotonic decrease in binding energy characteristic of the layer growth mode may cause the 2D to 3D growth transformation. As an example, the film–substrate lattice mismatch causes strain energy to accumulate in the growing film. The release of this energy from the deposit–intermediate layer interface may trigger the formation of the islands. This process is illustrated in Fig. 1.30, where the formation of InAs (lattice constant = 6.0564 Å) quantum dot on GaAs (lattice constant = 5.65321 Å) is illustrated.

1.4.1 Nucleation

There are a few theories dealing with nucleation. One is the capillarity theory, which is a simple qualitative model that describes the film nucleation. It does

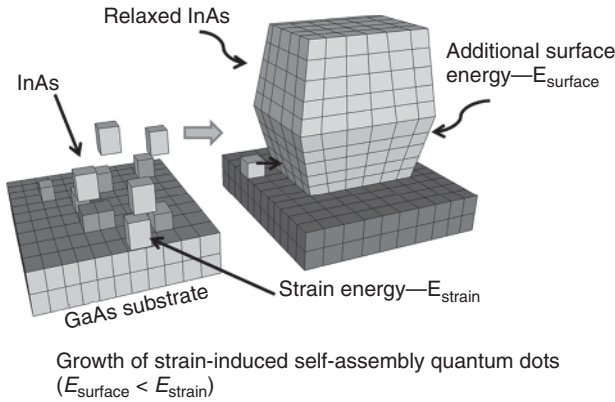


FIGURE 1.30 A schematic illustrates the formation of InAs quantum dot (island) on GaAs substrate.

not provide quantitative information since it lacks the detailed atomistic assumption. However, it provides attractive broad generality, where useful connections between variables, such as substrate temperature, deposition rate, and critical film nucleus size, can be deduced. Atomic nucleation processes theory, introduced by Walton *et al.*, is based on the atomistic approach to nucleation. It treats clusters as macromolecules and applies concepts of statistical mechanics in describing them. Another useful model is based on cluster coalescence and depletion. Brief descriptions of these three models are presented in this section.

1.4.1.1 Capillarity Theory Island formation is assumed when the atoms and molecules are impinging on the substrate. The change of the free energy accompanying the formation of islands of mean dimension r can be written as

$$\Delta G = \alpha_3 r^3 \Delta G_V + \alpha_1 r^2 \gamma_{vf} + \alpha_2 r^2 \gamma_{fs} - \alpha_2 r^2 \gamma_{sv}, \quad (1.50)$$

where ΔG_V is the chemical free energy change per unit volume which drives the condensation reaction, γ_{vf} is the interfacial tension between the vapor and the film, γ_{fs} is the interfacial tension between the film and the substrate, and γ_{sv} is the interfacial tension between the substrate and the vapor. The parameters, α_1 , α_2 , and α_3 , are geometric constants given by $2\pi(1 - \cos\theta)$, $\pi \sin^2\theta$, and $\pi(2 - 3\cos\theta + \cos^3\theta)/3$, respectively, for the nucleus shape shown in Fig. 1.31. The curved surface area is $\alpha_1 r^2$, and the volume is $\alpha_3 r^3$. The projected circular area on the substrate is $\alpha_2 r^2$. Young's equation between the interfacial tensions at equilibrium yields

$$\gamma_{sv} = \gamma_{fs} + \gamma_{vf} \cos\theta, \quad (1.51)$$

where the angle θ depends on the surface properties of the involved materials. The three growth modes described in Fig. 1.29 can now be distinguished according to

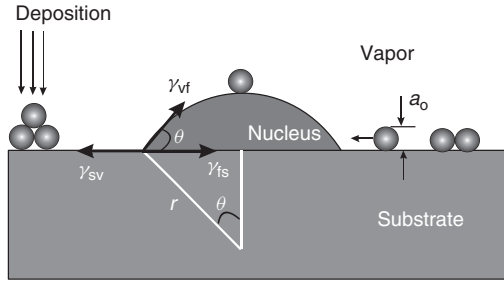


FIGURE 1.31 An illustration of the basic processes of vapor deposition on a surface of a substrate.

the following relationships between the interfacial tensions. For island (Volmer-Weber) growth mode, $\theta > 0$ which yields

$$\gamma_{sv} < \gamma_{fs} + \gamma_{vf}. \tag{1.52}$$

For layer growth (Frank-van der Merwe), the deposit wets the substrate and $\theta = 0$, hence

$$\gamma_{sv} = \gamma_{fs} + \gamma_{vf}. \tag{1.53}$$

An ideal homoepitaxy implies that $\gamma_{fs} = 0$, which yield $\gamma_{sv} = \gamma_{vf}$. The SK growth mode fulfills the inequality

$$\gamma_{sv} > \gamma_{fs} + \gamma_{vf}, \tag{1.54}$$

where the strain energy per unit area of film growth is larger than the interfacial tension between the vapor and film. This condition triggers the formation of quantum dots on the top of the wetting layer.

Figure 1.30 indicates that when a new interface appears there is an increase in the surface free energy. This implies that the second and third terms in Equation (1.50) are positive. The loss of the circular substrate–vapor interface under the film nucleus indicates, as shown in Fig. 1.31 a reduction of the system energy. Thus, the fourth term in Equation (1.50) is negative. The energy barrier to a nucleation process, ΔG^* , can be obtained by first finding the critical radius of the film nucleus. This critical radius, r^* , is obtained by evaluating $\partial \Delta G / \partial r = 0$. Second, substitute r^* backs into Equation (1.50) to obtain

$$\Delta G^* = \frac{4(\alpha_1 \gamma_{vf} + \alpha_2 \gamma_{fs} - \alpha_3 \gamma_{sv})^3}{27 \alpha_3^2 \Delta G_v^2}. \tag{1.55}$$

By substituting the geometrical factors, α_1 , α_2 , and α_3 into Equation (1.55), the energy barrier, ΔG^* , takes the following form

$$\Delta G^* = \left(\frac{16\pi \gamma_{vf}^3}{3 \Delta G_v^2} \right) \left(\frac{2 - 3 \cos \theta + \cos^3 \theta}{4} \right). \tag{1.56}$$

An island or aggregate smaller in size than r^* disappears by shrinking, thus lowering ΔG in the process. Equation (1.56) indicates that the heterogeneous nucleation depends on the angle θ . The second term in this equation is called the *wetting factor*. For $\theta = 0$, the wetting factor is zero, and for $\theta = \pi$, the wetting factor is unity. When the deposited film wets the substrate ($\theta = 0$), ΔG^* is zero and there is no barrier to nucleation. On the other hand, when the wetting factor is unity ($\theta = \pi$), ΔG^* is maximum and the growth is identical to that for homogeneous growth.

In the case where the strain energy per unit volume, ΔG_s , is considered in the analysis, the denominator of Equation (1.56) is modified to $3(\Delta G_v + \Delta G_s)^2$. The chemical free energy per unit volume, ΔG_v , is usually a negative quantity, while ΔG_s is a positive quantity. Thus, the overall energy barrier to nucleation is increased. If the substrate is initially strained, then release of this stress during nucleation would be indicated by a reduction in ΔG^* .

The nucleation rate, \dot{N} , is one of the parameters that has to be considered during quantum dot growth. According to the capillarity model, the nucleation rate can be written as

$$\dot{N} = N^* A^* \Phi \text{ nuclei}/(\text{cm}^2 \cdot \text{s}) \quad (1.57)$$

where N^* is the equilibrium concentration per square centimeter of stable nuclei, A^* is the nucleus critical area, and Φ is the overall impingement flux. The equilibrium number of nuclei of critical size per unit area on the substrate is given by

$$N^* = n_s e^{-\frac{\Delta G^*}{k_B T}}, \quad (1.58)$$

where n_s is the total nucleation site density, k_B is the Boltzmann constant, and T is the temperature. A certain number of these sites are occupied by monomers (adatoms) whose surface density, n_a , is the product of the vapor impingement flux and the adatom lifetime, τ_s , which is given by

$$n_a = \frac{\tau_s P N_A}{\sqrt{2\pi MRT}}, \quad (1.59)$$

and τ_s is the given by

$$\tau_s = \frac{1}{\nu} e^{\frac{E_{\text{des}}}{k_B T}} \quad (1.60)$$

where E_{des} is the energy required to desorb the adatom back into vapor, and ν is vibrational frequency of the atom ($\sim 10^{12} \text{ s}^{-1}$). The area of the nucleus, depicted in Fig. 1.31, can be expressed as

$$A^* = 2\pi r^* a_0 \sin \theta, \quad (1.61)$$

where a_0 and θ are defined in Fig. 1.32. The overall impingement flux is the product of the jump frequency and n_a , where the jump frequency is defined

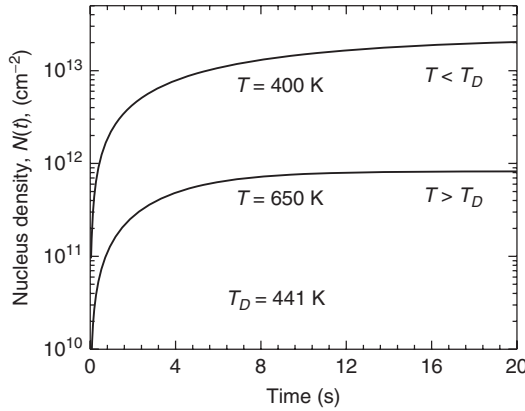


FIGURE 1.32 The nucleus density, $N(t)$, is obtained as a function of deposition time for both $T > T_D$ and $T < T_D$ using Equation (8.74).

as the adatom diffuse jumps on the substrate with a frequency given by $\nu \exp(-E_s/k_B T)$ and E_s is the activation energy of the surface diffusion. Thus, Φ can be expressed as

$$\Phi = \frac{\tau_s P N_A \nu e^{-\frac{E_s}{k_B T}}}{\sqrt{2\pi M R T}} (\text{cm}^{-2} \cdot \text{sec}). \quad (1.62)$$

Combine Equations (1.57), (1.58), (1.61), and (1.62) to obtain the following expression for the nucleation rate

$$\dot{N} = 2\pi r^* a_0 \sin \theta \frac{P N_A}{\sqrt{2\pi M R T}} n_s e^{\frac{(E_{\text{des}} - E_s - \Delta G^*)}{k_B T}} \text{nuclei}/(\text{cm}^2 \cdot \text{sec}). \quad (1.63)$$

The nucleation rate is a strong function of the desorption energy, surface diffusion energy, and nucleation energy.

1.4.1.2 Atomistic Nucleation Processes (Walton *et al.* Theory) The Walton *et al.* model of nucleation describes the role of individual atoms and the association of small numbers of atoms during the earliest stage of film formation. The model introduces the critical dissociation energy E_{i^*} , which is defined as the energy required to dissociate a critical cluster containing i atoms into i separate monomers. The critical concentration of clusters per unit area, N_{i^*} , is given by

$$\frac{N_{i^*}}{n_0} = \left| \frac{N_1}{n_0} \right|^{i^*} e^{\frac{E_{i^*}}{k_B T}}, \quad (1.64)$$

where n_0 is the total number of adsorption sites and N_1 is the monomer density, which can be written as

$$N_1 = \Phi \tau_s = \Phi \nu^{-1} e^{\frac{E_{\text{des}}}{k_B T}}, \quad (1.65)$$

where Φ and τ_s are defined earlier. The critical monomer supply rate is given by the impingement rate and the area over which the monomers are capable of diffusing before desorbing. This area, \mathcal{L}^2 , can be defined as

$$\mathcal{L}^2 = 2D_s\tau_s, \quad (1.66)$$

where \mathcal{L} is the diffusing mean distance and D_s is the surface diffusion coefficient given by

$$D_s = \frac{1}{2}a_0^2\nu e^{-\frac{E_s}{k_B T}}. \quad (1.67)$$

Thus, the critical monomer supply rate, $\Phi\mathcal{L}^2$, is given by

$$\Phi\mathcal{L}^2 = \Phi a_0^2 e^{\frac{(E_{\text{des}} - E_s)}{k_B T}}. \quad (1.68)$$

The critical nucleation rate, \dot{N}_{i^*} , can now be obtained by combining Equations (1.64)-(1.68) such as

$$\dot{N}_{i^*} = N_{i^*}\Phi\mathcal{L}^2 = \Phi a_0^2 n_0 \left| \frac{\Phi}{\nu n_0} \right|^{i^*} e^{\frac{\{(i^*+1)E_{\text{des}} - E_s + E_{i^*}\}}{k_B T}} \text{ (cm}^2 \text{ sec}^{-1}) \quad (1.69)$$

This expression has been used extensively in determining the nucleation rates in many materials including metals and semiconductors. One of the advantage of this model over the capillarity model is that the uncertainties are in i^* and E_{i^*} , while the uncertainties in the capillarity model are in more parameters (ΔG^* , γ , and θ).

Equation (1.69) can be used to predict the thermally activated nucleation rate whose energy depends on the size of the critical nucleus. This means that there are critical temperatures where the nucleus size and orientation undergo change. As an example, let us consider the temperature $T_{1 \rightarrow 2}$ at which there is a transition from one- to two-atom nucleus. This temperature can be obtained by equating the rates $\dot{N}_{i^*=1} = \dot{N}_{i^*=2}$, which leads to

$$T_{1 \rightarrow 2} = -\frac{E_{\text{des}} + E_{21}}{k_B \ln\left(\frac{\Phi}{\nu n_0}\right)} \quad \text{or} \quad \Phi = \nu n_0 e^{-\frac{E_{\text{des}} + E_{21}}{k_B T_{1 \rightarrow 2}}} \quad (1.70)$$

where $E_{21} = E_{i^*=2} - E_{i^*=1}$. According to Walton *et al.* when the cluster is composed of one atom, then $E_{i^*=1} = 0$. Thus, E_{21} is simply E_2 and E_{31} is E_3 and so on. As an example, let us assume that a deposition growth rate of a compound semiconductor on a substrate was obtained as a function of temperature. An Arrhenius plot of the data yields an activation energy of $(E_{\text{des}} + E_{21}) = 2.1$ eV. The deposition rate was estimated to be 1.0×10^{14} atoms/(cm/s) and $\nu n_0 = 7 \times 10^{27}$ atoms/(cm.sec). The critical transition temperature can now be calculated from Equation (1.70) to be ~ 764 K. The derivations of expressions for transitions from $i^* = 1$ to $i^* = 3$, $i^* = 1$ to $i^* = 4$, and $i^* = 2$ to $i^* = 4$ were left as an exercise.

Kinetic modeling of nucleation has been the subject of many complex mathematical and physical theoretical models in recent years. Detailed discussions of

these models are outside the scope of this textbook. However, the general form of the rate equation for clusters with size i is

$$\frac{dN_i}{dt} = K_{i-1}N_1N_{i-1} - K_iN_1N_i, \quad (1.71)$$

where N_i are the densities of clusters and K_i are the rate constants. The first term on the right-hand side represents the increase in the clusters size by attaching monomers to smaller ($i-1$) sized clusters. The second term expresses the decrease in the cluster density when it reacts with monomers to produce larger ($i+1$) sized clusters. There are i coupled rate equations to work with, each one of which depends directly on the impingement from the vapor as well as desorption through Equation (1.65). The addition of diffusion terms ($\partial^2 N_i / \partial x^2$) to these coupled equations allows one to account for the change in the cluster shape. A more complete nucleation event can be obtained by including the cluster mobility and coalescence.

Robinson and Robins presented a model for the nucleation and growth kinetics for a one-atom critical nucleus ($i^* = 1$). They considered two temperature regimes separated by a characteristic temperature, T_D , given by

$$T_D = \left| \frac{2E_s - 3E_{\text{des}}}{k_B \ln[(C\alpha^2/\beta)(\Phi/vn_0)]} \right|, \quad (1.72)$$

where C is a number of pair formation sites ($C = 4$ for a square lattice) and α and β are dimensionless constants with typical values of 0.3 and 4, respectively. For temperatures higher than T_D , the reevaporation rate from the surface will control the adatom density and exceed the rate of diffusive capture into growing nuclei. In this regime, the adsorption–desorption equilibrium is rapidly established where $N_1 = \Phi\tau_s$ and incomplete condensation is said to occur. The second regime, where the temperatures are lower than T_D , is characterized by high desorption energy (E_{des}) and reevaporation is insignificant. Thus, the condensation is complete and the monomer capture rate by growing nuclei exceeds the rate at which they are lost due to desorption (evaporation).

The analytical expressions for the time-dependent transient density of stable nuclei, $N(t)$, and the saturation value of $N(t = \infty) = N_s$ are given as follows

$$N(t) = \begin{cases} N_s \tanh \left(\frac{\dot{N}(0)t}{N_s} \right) & \text{for } T > T_D \\ N_s \left\{ 1 - e^{-3\eta^2 \frac{\dot{N}(0)t}{N_s^3}} \right\} & \text{for } T < T_D \end{cases} \quad (1.73)$$

$$N_s = \begin{cases} \sqrt{Cn_0/(\beta v)} \sqrt{\Phi} e^{\frac{E_{\text{des}}}{2k_B T}} & \text{for } T > T_D \\ (Cn_0^2/(\alpha\beta v))^{1/3} \Phi^{1/3} e^{\frac{E_s}{3k_B T}} & \text{for } T < T_D \end{cases} \quad (1.74)$$

where

$$\dot{N}(0) = \left. \frac{\partial N(t)}{\partial t} \right|_{t=0} = \frac{C\Phi^2}{vn_0} e^{\frac{2E_{\text{des}} - E_s}{k_B T}}, \quad (1.75)$$

TABLE 1.5 Nucleation Parameters P and E in Equation (1.77) as Reported by Venables *et al.* for Different Regimes

Regime	Three Dimensional	Two Dimensional
Extreme incomplete	$P = 2i^*/3$	$P = i^*$
	$E = (2/3)\{E_{i^*} + (i^* + 1)E_{\text{des}} - E_s\}$	$E = E_{i^*} + (i^* + 1)E_{\text{des}} - E_s$
Initially incomplete	$P = 2i^*/5$	$P = i^*/2$
	$E = (2/5)\{E_{i^*} + i^*E_{\text{des}}\}$	$E = (1/2)\{E_{i^*} + i^*E_{\text{des}}\}$
Complete	$P = i^*/(i^* + 5/2)$	$P = i^*/(i^* + 2)$
	$E = \{E_{i^*} + i^*E_s\}/(i^* + 5/2)$	$E = \{E_{i^*} + i^*E_s\}/(i^* + 2)$

and

$$\eta = \frac{n_0}{\alpha} e^{\frac{E_s - E_{\text{des}}}{k_B T}}. \quad (1.76)$$

These equations indicate that $N(t)$ increases with time and reaches saturation at the value N_s . Let us consider the deposition of clusters of a material where $E_s = 0.29$ eV and $E_{\text{des}} = 0.7$ eV. The rest of the parameters are $n_0 = 5 \times 10^{15}$ cm⁻², $\nu = 1.65 \times 10^{12}$ sec⁻¹, $C = 4$, $\alpha = 0.3$, $\beta = 4$, $\Phi = 8.5 \times 10^{14}$ nucleus/(cm/s). The characteristic temperature is calculated from Equation (1.72) to be $T_D = 441.0$ K. The cluster (nucleus) density $N(t)$ is calculated from Equation (1.73) for the following temperatures $T = 700$ K (larger than T_D) and $T = 430$ K (smaller than T_D). The results are shown in Fig. 1.32. It is clear from this figure that the number of nuclei (clusters) is larger when the deposition temperature, T , is smaller than the characteristic temperature T_D . When $T > T_D$, the desorption process (reevaporation rate) dominates over the condensation process. This leads to a lower cluster density as compared to the case when $T < T_D$.

For the case where i^* is any integer, the analysis becomes complicated. However, a review article on the subject was presented by Venables *et al.* in which the nucleation parameters for 3D and 2D were summarized. The stable cluster density is given by Venables *et al.* as

$$N_s = An_0 \left| \frac{\Phi}{\nu n_0} e^{\frac{E}{k_B T}} \right|, \quad (1.77)$$

where A is a dimensionless constant that depends on the substrate coverage. The parameters P and E depend on the condensation regimes, which are summarized in Table 1.5.

The complete and extreme incomplete regimes are similar to those discussed earlier. The extreme incomplete regime occurs when the reevaporation process (desorption) is dominant, and the complete regime occurs when the monomers capture rate exceeds the desorption rate. The initially incomplete regime can be thought of as an intermediate regime which is applicable to SK growth mode.

1.4.1.3 Cluster Coalescence, Sintering, and Migration Models According to the kinetic models, the initial stages of growth are characterized by an increase in the density of the stable clusters as a function of growth time until it reaches a maximum level before starts to decrease (saturation effect). The process that describes the cluster behavior beyond saturation is called *coalescence*. This coalescence process is usually characterized by a decrease in the total number of clusters and an increase in the height of surviving clusters. Other features that describe the coalescence process include the following: clusters with well-defined crystallographic facets tend to become rounded; the clusters take a crystallographic shape with time; the process appears to be liquidlike in nature with clusters merging and changing shapes, where the crystallographic structure of the larger clusters dominates during the merger of smaller clusters; and the clusters are observed to migrate prior to their merger into one another.

There is a size variation when clusters are deposited on the surface of a substrate. The larger clusters tend to grow in size with time at the expense of the smaller ones. This is called *ripening effect*. The time evolution of cluster distribution was investigated by Vook using both statistical models involving single atom process and macroscopic surface diffusion-interface transfer models.

The coalescence process occurs by several methods. One method is called *Ostwald ripening* where the diffusion of adatoms will proceed from the smaller to larger cluster until the smaller cluster disappears completely. The diffusion of atoms occurs without having the clusters in direct contacts. A second method is called *sintering*, where the clusters are in contact. A neck is formed between the clusters and then thickens as the atoms are transported in the contact region. Cluster migration is another mechanism for coalescence where the clusters on the surface of the substrate actually migrate. Coalescence occurs in this mechanism as a result of collisions between separate clusters (droplet) as they randomly move around.

1.4.2 Fabrications of Quantum Dots

The production of low dimensional semiconductor systems, where the charge carriers are confined in two directions (quantum wires) and/or three dimensions (quantum dots), is of interest to those who are involved in the basic understanding of the nature of these systems, as well as those who are interested in producing devices based on the novelty of these quantum structures. Since the early 1980s, many research groups throughout the world have been focused on the production of quantum wires and dots using lithograph techniques. All the early efforts were focused on processing quantum wells into quantum wires or quantum dots by patterning. While, in many cases, the patterned techniques have proven to be difficult or expensive to perform, they offer several advantages, such as good control on the lateral shape, size, and arrangement.

Optical lithography techniques using lasers and ultraviolet optics in conjunction with photoresists are used to produce quantum dots with a resolution as high as 100 nm. This technique may not be able to reach dimensions on the order of

20 nm or less. However, X-ray has the potential to mass produce nanostructures, since it has a shorter wavelength.

Electron beam lithography has been used to produce quantum dots and wires. The electron beam is usually emitted from a high brightness cathode or a field emission gun. Since electrons are charged, it is very easy to focus them with magnetic lens system. A resolution of 10–20 nm has been achieved by this technique. The electron beam is computer controlled, and images can be defined on the substrate with the help of deflection fields system. The final resolution of the pattern is limited by the resists due to finite length of the organic molecules and the grain size. Periodic nanostructures can be produced by using electron beam interference technique.

In addition to electron beam lithography, focused ion beam lithography has been used in production of patterned quantum dots. This technique has been used for maskless etching, maskless implantation of dopants, deposition of metallic structures, and patterning of resists. However, the resolution of the focused ion beam lithography is not as high as the electron beam lithography. There are many other techniques used to pattern quantum dots or grow quantum dots on patterned substrate. For a detailed review of the subject, see Bimberg *et al.*

1.4.3 Epitaxial Growth of Self-Assembly Quantum Dots

The growth of self-assembly quantum dots has been widely made by MBE and MOCVD techniques. Our knowledge of the quantum dots structural characteristics has been obtained by tools, such as scanning electron microscopy (SEM), STM, atomic force microscopy (AFM), transmission electron microscopy (TEM), RHEED images, and X-ray diffraction. AFM has an atomic resolution, and the limiting factor of AFM is the size and shape of the microscope tip. The STM, on the other hand, has the advantage of revealing the morphology of a surface on an atomic scale. It also allows the manipulation of the surface atoms by lining them up and forming shapes and figures.

One of the most important aspects of quantum dot growth is the starting surface of the substrate. The surface construction, surface strain, and crystallographic orientations of the substrate play a major role in the growth of self-assembly quantum dots. As an example, let us consider the formation of InAs quantum dots on a GaAs (001) surface. In this case, the RHEED image exhibits a streaky pattern before the deposition of InAs atoms indicating a flat surface. RHEED pattern remains streaky before the 2D–3D transition occurs, which corresponds to 1–1.5 monolayer deposition of InAs. When more InAs atoms are deposited, the RHEED pattern changes from streaky to spotty, which is an indication of 3D islands being formed. Generally speaking, a monolayer of InAs remains stable for a short growth interruption time on the order of 10 s or so. As the growth interruption continues (more than 1000 s), the InAs material transitions into 3D islands with anisotropic shapes and sizes.

A simple model was presented by Leonard *et al.*, where the 3D islands start to develop on top of a 2D wetting layer above a critical thickness, Θ_c . The planar

density of the MBE-grown InAs 3D islands, ρ_{SAD} , was determined from AFM images versus the amount of InAs deposited, Θ . The relation between ρ_{SAD} and Θ was described as being similar to that of a first-order phase transition

$$\rho_{\text{SAD}} = \rho_0(\Theta - \Theta_c)^\alpha, \quad (1.78)$$

where α is the exponent and ρ_0 is the normalization density. A fit of the results is shown in Fig. 1.33 using Equation (1.78), which yields $\alpha = 1.76$ and $\rho_0 = 2 \times 10^{11} \text{ cm}^{-2}$.

Since Leonard *et al.* reported their finding, several research groups have investigated the 2D to 3D transition in many quantum dot systems and their reports provided complex structures and behaviors depending on the growth temperature, substrate starting surface, and crystallographic orientations. For example, AFM images of various self-assembled quantum dots grown by the MBE technique are shown in Fig. 1.34. The quantum dot size and density depend strongly on the growth temperature and post-growth annealing. An illustration of these effects on InAs quantum dots is shown in Fig. 1.35, where the growth temperature (substrate temperature) varied from 400°C to 500°C at a fixed deposition time of 20 s. The quantum dots were MBE grown on $\sim 0.20 \mu\text{m}$ thick AlAs (lattice constant = 5.660 Å) layer, which was grown on a GaAs substrate. The InAs growth rate was $\sim 0.30 \text{ \AA/s}$, which yields a total deposited material of ~ 2 monolayers. The quantum dot density decreases as the growth temperature increases. Accompanying the decrease in density is an increase in the quantum dot size, as shown in Fig. 1.35a. The post-growth annealing has a similar effect. Figure 1.35b shows STM images of the same sample that was grown at 500°C but annealed as a function of time. In this case, the density of the quantum dots decreases and their size increases as

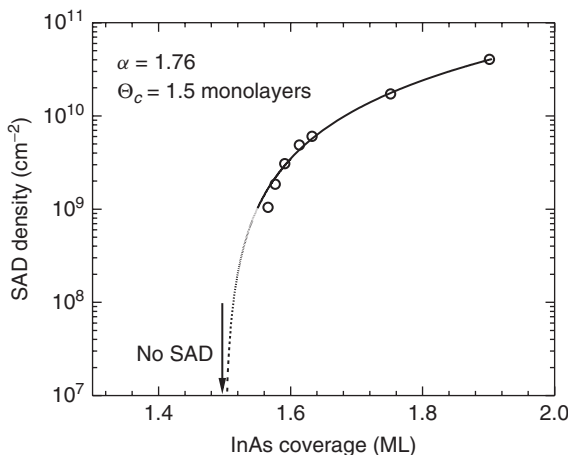


FIGURE 1.33 Density of self-assembled dots (SAD) versus InAs coverage. Treating these data as a first-order phase transition gives a critical thickness of 1.50 monolayers (ML) (after Leonard *et al.*).

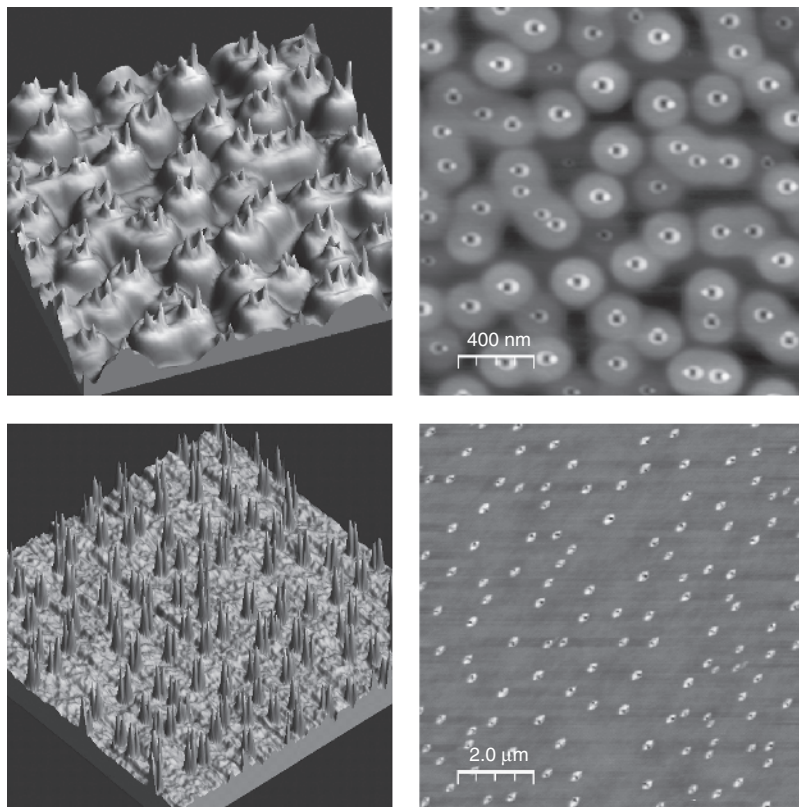
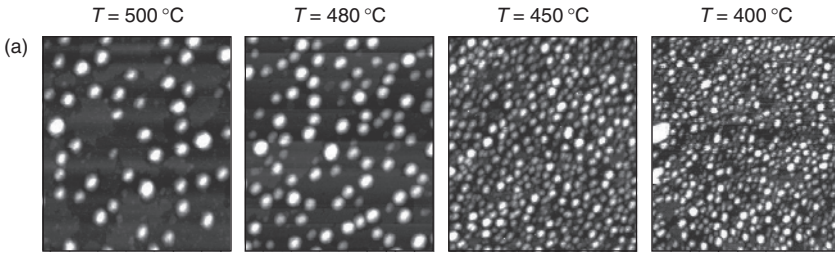


FIGURE 1.34 Atomic force microscopy images of different types of quantum dots grown by the molecular beam epitaxy.

the annealing time is progresses from $t = 0$ to $t = 10$ min. The behavior of the quantum dots as a function growth temperature and post-growth annealing time can be understood in terms of the kinetics model discussed in Section 1.4.1.

The growth of quantum dots is highly influenced by the growth conditions. The growth temperature and post-growth annealing discussed above are examples of how the density and size of the quantum dots are drastically changed. There are many other parameters that affect the structural and physical properties of quantum dots. The growth modes such as the simultaneous deposition mode and alternate deposition modes can yield different results. In the simultaneous deposition mode, the constituent atoms are deposited at the same time. This is accomplished by opening the sources shutters at the same time. On the other hand, the alternative deposition mode relies on the alternative deposition of the constituents of the quantum dots. Quantum dots grown by the simultaneous deposition mode were found to be affected by the quantum dot arrangement on the surface of the substrate, while the alternative deposition mode produces higher densities of quantum dots grown on vicinal substrates.

Effect of substrate temperature T ($t = 20\text{s}$)



Effect of annealing time t ($T = 500\text{ °C}$)

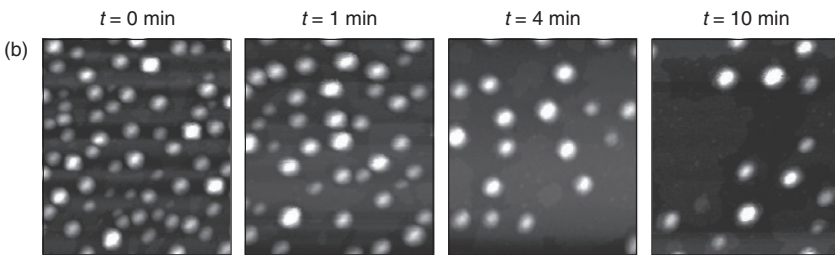


FIGURE 1.35 Illustration of the growth temperature and post-growth annealing effects on InAs quantum dots grown by MBE on AlAs layer, which was grown on GaAs (001) substrate. (a) An STM images obtained for different samples that were grown at different temperatures. (b) The STM image illustrates the post-growth annealing on the quantum dots size and density as the annealing time is increased.

Arsenic pressure in the MBE growth of InAs affects the stability of the quantum dots. An increase of the arsenic pressure in the MBE chamber can dramatically affect the morphology of the quantum dots. The size of the quantum dots is reduced, and significant dislocation densities appear in larger InAs clusters. The arsenic pressure can also affect the transitions from 2D to 3D growth. The stoichiometry of (001) surfaces of III–V compound semiconductors that are in equilibrium with the gas is known to depend on the partial pressure of group V elements. Thus, a change in the arsenic pressure leads to a change in the surface reconstructions and to a change in the surface energy of the GaAs (001) surface. At a lower arsenic pressure, indium is known to segregate to the surface, which can be regarded as a quasi-liquid phase that shows no strain-induced renormalization of surface energy. Thus, an increase in the surface area due to the arsenic pressure reduction may lead to a large surface energy making the formation of 3D islands unfavorable.

Substrate orientation plays a vital role in the growth and formation of the quantum dot systems. It affects all parameters governing the quantum dot formation, such as strain energy and surface energy. The strain caused by the difference of the lattice constants of the quantum dots and the substrate is the primary reason for the formation of self-assembled quantum dots. Additionally, this strain

difference affects the electrical and optical properties of the quantum dot systems. For homoepitaxial growth, the lattice constants of the epitaxial film and the substrate are identical and strain does not exist in the grown film. For heteroepitaxial growth, the film being deposited on a substrate does not necessarily have a lattice constant similar to that of the substrate. Owing to this lattice constant difference, one can envision three distinct epitaxial cases, which are illustrated in Fig. 1.36. The first case is when there is a lattice match or a very small lattice mismatch between the deposited film and the substrate as shown in Fig. 1.36a. The strain in this case is almost zero, and the heterojunction growth is identical to the homoepitaxial growth. The second case is when there is a lattice mismatch between the film and the substrate. This lattice mismatch causes the strain in the film as shown in Fig. 1.36b. A small lattice mismatch is actually beneficial for many heterojunction systems where the mechanical and optoelectronic properties are enhanced by the strain. Strain usually removes the degeneracy, which leads to an improvement in the electronic and optical properties of the film. In fact, the presence of this strain in the deposited material is the driving mechanism for the formation of self-assembled quantum dots. When the lattice mismatch is substantially large, the thin film is relaxed by the formation of the dislocations at the interfaces as shown in Fig. 1.36c. The relaxed epitaxy is usually reached during later film formation stage (thicker films) regardless of the crystal structures or lattice constant difference. For all quantum dot systems, the dots are strained.

In addition to planar self-organization of quantum dots, the quantum dots can be vertically stacked. The vertical stacking is very important for devices, such as detectors and emitters, since this stacking increases the filling factor of quantum dots. Depending on the growth temperature and the spacer or barrier, the physical, structural, and morphological properties of the vertically stacked quantum dots can be different than those of the planar self-organized dot systems. An illustration of the vertical stacked quantum dots is shown in Fig. 1.37 for InGaAs/GaAs system. The images were obtained using TEM for both the planar and the cross-section (X-TEM) configurations. A remarkable property of the vertically stacked quantum dots is that the dots are self-aligned vertically as it is clearly shown in the cross-sectional TEM images. The vertical correlation has been observed in many quantum dot systems, and it can be lost if the barrier thickness is too large. For vertical self-alignment to occur, it is very important that the quantum dot layer is successfully grown.

The planar TEM image shown in Fig. 1.37 clearly demonstrates the formation of the InGaAs quantum dot chains grown on GaAs (001) surface. The quantum dots shape in the first layer is not well defined. By inspecting the X-TEM image of the quantum dot stack, the quantum dot shape is not well defined in the first layer, but then subsequent layers show that the shape of the quantum dots are well defined and pyramidal in shape.

Additionally, the size of the quantum dots becomes uniform as the multiple layers of quantum dots are stacked. The production of quantum dots uniform in size is a very important and necessary aspect of nanotechnology, since the uniformity of the dots affects the device performance. The size fluctuation impacts the

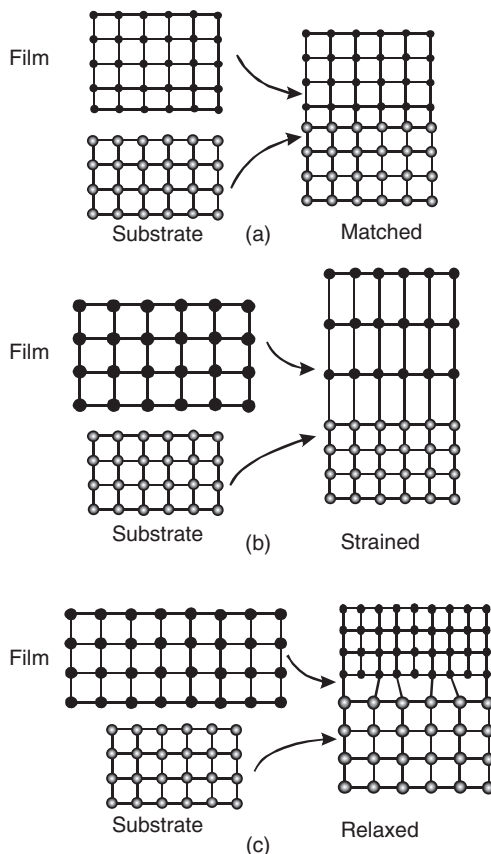


FIGURE 1.36 A sketch of heterojunction growth showing (a) lattice matched, (b) strained, and (c) relaxed structures.

quantized energy levels in the dots causing inhomogeneous energetic broadening. This broadening should be minimized by producing quantum dots with highly uniform size. For example, infrared detectors fabricated from quantum dots usually require structures that are composed of multiple layers of dots and barriers. This structure is required to obtain a minimum number of dots. The detection of light relies on the confined energy levels inside the quantum dots. The positions of these energy levels are very sensitive to the physical dimensions of the dots.

1.5 COLLOIDAL GROWTH OF NANOCRYSTALS

Colloidal growth technique has many variations depending on the type and properties of the nanocrystal. The most common techniques are sol–gel, hydrothermal synthesis, solvothermal synthesis, emulsion, high temperature organic solvent,

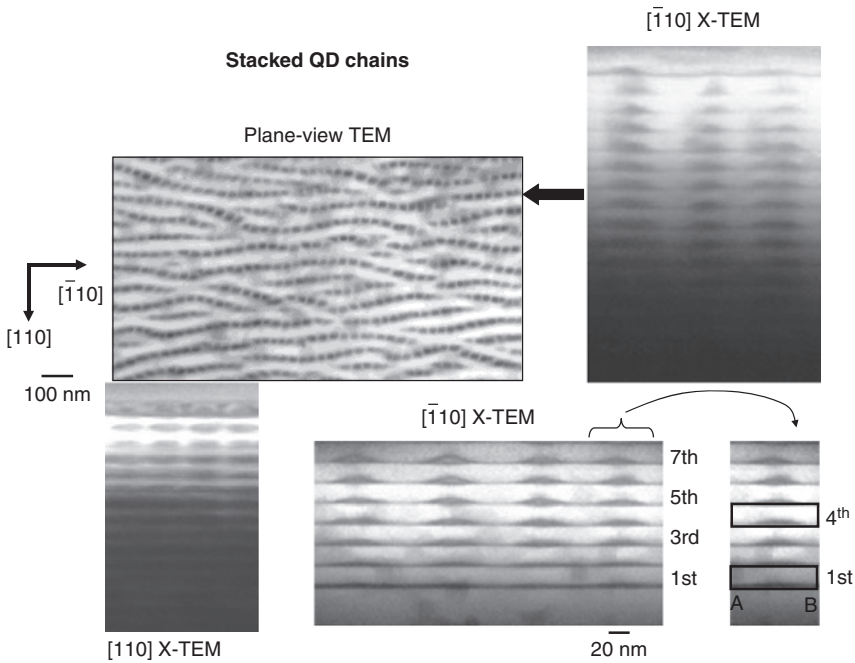


FIGURE 1.37 Tunneling electron microscopy images of InGaAs/GaAs multiple quantum dot layers. The planar view shows the formation of quantum dot chains, while the cross-sectional images show the vertical correlation of the quantum dots.



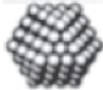
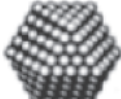


and co-precipitations. Colloidal growth produces all kind of nanomaterials including metals, semiconductors, and oxide nanoparticles with different shapes and sizes. These colloidal nanocrystals are usually uniform in sizes and properties make them ideal nanomaterials for many applications, such as light emitting diodes and detectors. The percentage of the surface atoms of the nanocrystals is very large depending on the number of the complete shells in the crystal. This is demonstrated in Table 1.6. When the nanocrystals are not stable, a shell from a different stable material is grown leading to what is called core/shell nanocrystals, such as CdSe/ZnS, InP/ZnS, and CdSe/CdS core/shell nanocrystals. The diameters of these nanocrystals are usually ranging between 2 and 30 nm or so.

The optical and electrical properties of the nanocrystal strongly depend on their size. For example, the effective band gap energy (E_g^*) of the nanoparticles is red shifted as the size of the nanocrystal is increased according to the following relationship:

$$E_g^* = E_g + \chi \left(\frac{\pi^2 \hbar^2}{2\mu^* d^2} \right), \quad (1.79)$$

where E_g is the band gap energy of the bulk materials, \hbar is Planck's constant, μ^* is the reduce effective mass of the materials, which depends on the electron (m_e^*) and hole (m_h^*) effective masses ($1/\mu^* = 1/m_e^* + 1/m_h^*$), d is the diameter

TABLE 1.6 The Relationship between the Total Number of Atoms in Full-Shell Clusters and the Percentage of Surface Atoms

Crystal	Number of Shells	Diameter Å	Number of Atoms	Surface Atoms (%)
	One shell	6.0	13	92
	Two shells	10	55	76
	Three shells	14	147	63
	Four shells	18	309	52
	Five shells	22	561	45
	Six shells	26	1415	35

Courtesy of A. Wang.

of the nanocrystal, and χ is a numerical factor which is close to unity for ideal nanocrystals. A plot of the effective band gap as a function of the nanocrystal diameter for different materials is left as an exercise (Problem 1.20).

The cost of the nanocrystals' growth is usually very low as compared to the growth cost by using MBE and MOCVD techniques. Since the nanocrystal growth depends on many chemical reactions, these nanocrystal are usually covered with ligands called *trioctylphosphineoxide* (TOPO). Ligands removal or exchange is very necessary to functionalize the nanocrystals for device applications, such as light emitting device, detectors, sensors, and photovoltaic device.

1.6 SUMMARY

The basic principles of single-crystal growth ranging from bulk semiconductor materials to quantum dots and nanocrystals are discussed. The introduction of this chapter is focused on the importance of bulk materials and the wafering process.

The growth of any materials, elemental or compound, depends on a set of thermodynamic conditions. The phase diagram is a critical aspect in understanding the thermodynamic conditions needed to grow single-crystal materials.

In addition to many bulk semiconductor applications, single-crystal wafers are vital to the growth of thin films and the epitaxial growth of all nanomaterial structures including heterojunctions, quantum wells, quantum wires, and quantum dots. Thus, understanding the growth of bulk semiconductors is essential to this chapter. The most widely used bulk growth methods were discussed, including LEC, Bridgman, float zone, and Lely methods. The segregation coefficient of dopants in bulk material is discussed. The elimination of background impurities or the introduction of a well-controlled dopant in bulk materials are very important. The dopant distribution in bulk semiconductor crystals is usually depends on the radius and the length of the boules.

There are several methods used to grow semiconductor thin films on substrates and wafers. The most common methods used in the growth of thin films are LPE, VPE, HVPE, PLD technique, MBE, and MOCVD technique. Each one of these techniques has advantages and disadvantages, which are briefly discussed in this chapter.

Epitaxial growth rate, nucleation, and growth kinetics of highly nonequilibrium growth were discussed. Several nucleation models were reported to explain the three island nucleation. The CVD growth technique is discussed. This technique is usually used to grow nanorods and nanotubes. The colloidal growth of nanocrystals was briefly discussed. These nanomaterials have myriad applications, ranging from optoelectronic devices to medical diagnosis.

PROBLEMS

- 1.1.** Find the miller indices for a plane intercepting the following crystal coordinates:

$$1a, -2a, 3a$$

$$2a, \infty, \infty$$

$$\infty, 3a, 5a$$

$$\infty, \infty, -1a$$

$$1a, 1a, 1a$$

where a is the interatomic distance also known as the *lattice constant*.

- 1.2.** Draw the crystal planes for the following orientations: (200), (222), (311), (133), and (123).
- 1.3.** What are the total number of planes of the following groups: {001}, {011}, and {111}. Show all the possible orientations for each group
- 1.4.** Derive Equation (1.6). Calculate ΔG° for a chemical reaction at $T = 300$ K with $k = 2.3 \times 10^{-9}$.
- 1.5.** Derive Equation (1.8). Calculate the maximum velocity in inches per hour needed to grow silicon single crystal. Assume the following parameters: $L = 340$ cal/g, $M_v = 2.33$ g/cm³, $dT/dx = 6$ K/cm, and $k_s = 0.21$ W/cm/K.
- 1.6.** Derive Equation (1.13) and plot C_s/C_0 versus m/m_0 for the following values of $k_0 = 0.01, 0.05, 0.3, 0.5, 0.9, 1, 2,$ and 3 .

- 1.7. Derive Equation (1.21).
- 1.8. Derive Equation (1.26), then plot C_s/C_0 as a function of x/L for the following values of $k_e = 0.01, 0.1, 0.5, 2,$ and 5 .
- 1.9. Calculate the mean-free path of an atom of a diameter of 2.5 \AA in an MBE chamber with a vapor pressure of 7.5×10^{-4} Torr. The substrate temperature is kept at 550°C . Compare your result to the typical source–substrate distance of 30 cm .
- 1.10. Show that the volume of flow of a gas escaping a container through an opening of an area \mathcal{A} into a region where the gas concentration is zero is given by

$$\dot{V} = 3.64 \times 10^3 \sqrt{T/M} \mathcal{A} \text{cm}^3 \cdot \text{sec}^{-1}$$

where T is the temperature and M is the atomic weight of the gas. Calculate the volume flow rate of a gas at 300 K and an atomic mass of 30 g/mole .

- 1.11. Show that the gas impingement flux, Φ , can be written as $\Phi = \frac{1}{4} \mathcal{N} \bar{v}$, where \mathcal{N} is molecules concentration and \bar{v} is the average velocity of the molecules. Consider the following form for the velocity distribution function: $f(v) = \frac{4}{\sqrt{\pi}} \left(\frac{M}{2RT}\right)^{3/2} v^2 e^{-\frac{Mv^2}{2RT}}$.
- 1.12. Derive Equation (1.49). A plot of this equation as a function of distance, x , for Si layer is shown in Fig. P1.12. The following conditions: $\bar{v} = 10 \text{ cm/sec}$, $C_i = 3 \times 10^{-6} \text{ g/cm}^3$, $b = 1.5 \text{ cm}$, $\rho = 2.3 \text{ g/cm}^3$, and $m_{\text{Si}}/m_s = 0.0205$. What would be the value of D needed to generate Fig. P1.12.

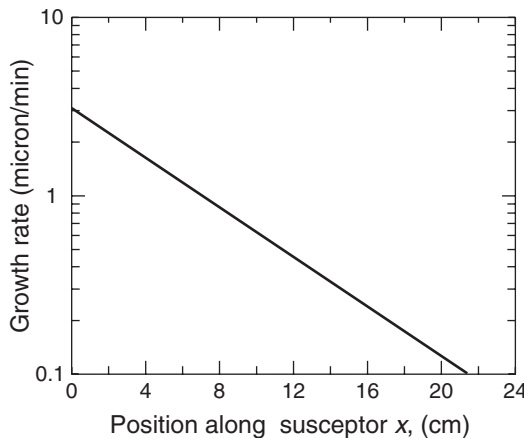
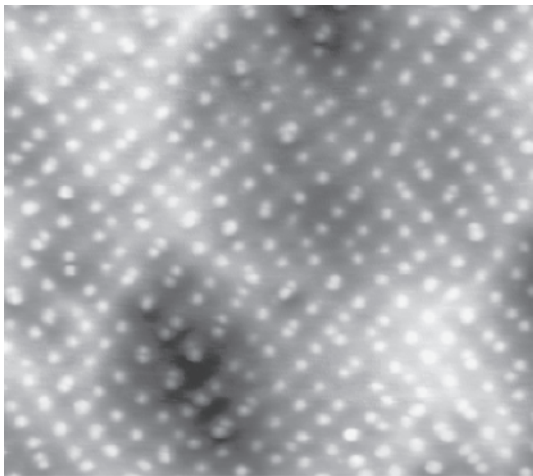


Fig. P1.12

- 1.13. Derive the expression of the barrier energy, ΔG^* , given by Equation (1.55). Show that this expression can be reduced to the form shown in Equation (1.56). Plot ΔG^* in Equation (1.56) as a function of the angle, θ , assuming that the first term in the right-hand side of the equation is unity.
- 1.14. The free energy change per unit thickness for a cluster of radius r is given by $\Delta G = \pi r^2 \Delta G_V + 2\pi \gamma r + A - B \ln(r)$, where $A - B \ln(r)$ is the energy contributed from dislocations within the cluster. Determine the

critical radius r^* and the nucleation barrier energy ΔG^* . Sketch ΔG versus r for the following parameters (assume unitless): $\pi \Delta G_V = -10$, $2\pi\gamma = 50$, $A = 10$, and $B = 0.1$. From the sketch shows the locations of r^* and ΔG^* .

- 1.15.** Derive Equation (1.69). Then obtain expressions for the critical temperatures at which the following transitions occur for one- to three-atom nucleus, one- to four-atom nucleus, and two- to three-atom nucleus.
- 1.16.** Consider the kinetics of one-atom critical nucleus where $E_s = 0.2$ eV and $E_{des} = 0.8$ eV, $n_0 = 5 \times 10^{15}$ cm $^{-2}$, $\nu = 0.10 \times 10^{12}$ sec $^{-1}$, $C = 4$, $\alpha = 0.3$, $\beta = 4$, and $\Phi = 1.0 \times 10^{14}$ nucleus/cm 2 .sec $^{-1}$. Calculate the characteristic temperature T_D using Equation (1.72). Plot the clusters (nucleus) density $N(t)$ as a function of time for $T = 730$ K and $T = 530$ K.
- 1.17.** Consider the following relations between the free energy, $\Delta G(i^*)$ and the number of atoms, i^* , in 3D deposited clusters on a surface of a substrate. $\Delta G(i^*) = -i^*\Delta\mu + (i^*)^{2/3}\chi$, where $\Delta\mu$ is the chemical potential energy and $\chi = 3.9$ eV is the surface free energy. Derive expressions for r^* and $\Delta G^*(i^* = r^*)$ from $\Delta G(i^*)$, where r^* is the critical number of atoms in the 3D clusters. Plot $\Delta G(i^*)$ vs. i^* for $\Delta\mu = -1, 0, 1$, and 2 eV. From the graph, find the values of $\Delta G^*(i^* = r^*)$ and the critical number of atoms, r^* , in the clusters for each value of $\Delta\mu$. When you plot $\Delta G(i^*)$ vs. i^* , use the limits of 0–100 atoms for i^* .
- 1.18.** The image shown here is an SEM image of InAs quantum dots grown on GaAs. The dimension of the image is $1 \mu\text{m} \times 1 \mu\text{m}$. Determine the quantum dots density in units of dots/cm 2 .



- 1.19.** Assume that the dimensions of the STM images of InAs quantum dots in Fig. 1.35 are $0.5\mu\text{m} \times 0.5 \mu\text{m}$. Estimate the quantum dots density (ρ) in

cm^{-2} in all images. Plot ρ as a function of the growth temperature and as a function of the annealing time.

- 1.20.** Plot the effective band gap energy as a function of the nanocrystal diameters in nanometers for the nanocrystals fabricated from the following materials.

Materials	E_g	m_c^*/m_0	m_h^*/m_0	χ
CdSe	1.75	0.11	0.45	0.75
CdS	2.48	0.14	0.51	0.80
ZnS	3.84	0.34	0.49	0.60
GaAs	1.52	0.067	0.45	0.70
InP	1.42	0.077	0.60	0.90
GaN	3.45	0.20	0.80	0.80
ZnO	3.43	0.28	0.59	0.70

BIBLIOGRAPHY

- Belyaev LM. Rubby and sapphire. New Delhi: Amerind Publishing Co.; 1980, translated from Russian, RUBIN I SAPFIR. Moscow: Nauka Publishers; 1974.
- Bimberg D, Grundmann M, Ledentsov NN. Quantum dot heterostructures. New York: John Wiley & Sons, Inc; 1999.
- Cho AY. Thin Solid Films 1983;100:291.
- Gith J, Petusky WT. J Phys Chem Solids 1987;48:541 (1987).
- Huang T-F, Harris SJ Jr. In: Manasreh MO, Ferguson IT, editors. Volume 19, III-nitride semiconductor growth. New York: Taylor & Francis; 2003. Chapter 10.
- Liu L, Edgar JH. Substrates for gallium nitride epitaxy. Mater Sci Eng 2002;R37:61.
- Manasreh MO, Ferguson IT. III-nitride semiconductors growth. New York: Taylor & Francis; 2003.
- Morkoç H. Handbook of nitride semiconductors and devices. Amsterdam: Springer-Verlag; 1999.
- Moustakas TD. Volume 57, Semiconductors and semimetals. New York: Academic; 1999. p. 33.
- Oda O, Fukui T, Hirano R, Muchida M, Kohiro K, Kurita H, Kainosho K, Asahi S, Suzuki K, Manasreh MO. InP and related compounds. New York: Taylor & Francis; 2000. Chapter 2.
- Ohring M. The materials science of thin films. New York: Academic; 1992. Chapter 4.
- Paskova T, Monemar B, Manasreh MO, Ferguson IT. Volume 19, III-nitride semiconductor growth. New York: Taylor & Francis; 2003. Chapter 6.
- Pfann WG. Zone melting. 2nd ed. New York: John Wiley & Sons, Inc; 1966.
- Razeghi M. Volume 1, The MOCVD challenge. Bristol: IOP Publishing Ltd.; 1989.
- Venables JA, Spiller GDT, Hanbücken M. Rep Prog Phys 1984;47:399.
- Vook RW. Int Met Rev 1982;27:209.
- Walton D, Rhidin TN, Rollins RW. J Chem Phys 1963;38:2698.